THE EFFECT OF UNCERTAINTY IN "FIELD OF THE DAY" TREATMENT REGIMES IN PROTON THERAPY

A Dissertation

presented to

the Faculty of the Graduate School

at the University of Missouri-Columbia

In Partial Fulfillment

of the Requirements for the Degree

Doctor of Philosophy

---

by

KEVIN GRANTHAM

Dr. Eric Klein, Dissertation Supervisor

Dr. Tushar Ghosh, Dissertation Supervisor

DECEMBER 2015

The undersigned, appointed by the dean of the Graduate School, have examined the dissertation entitled

THE EFFECT OF UNCERTAINTY IN “FIELD OF THE DAY” TREATMENT REGIMES IN PROTON THERAPY

presented by Kevin Grantham,

a candidate for the degree of doctor of philosophy,

and hereby certify that, in their opinion, it is worthy of acceptance.

Professor Eric Klein

Professor Tushar Ghosh

Professor Sudarshan Loyalka

Professor Mark Prelas

Professor Robert Tompson

Professor S. Murty Goddu

Professor Lixin Ma

ACKNOWLEDGEMENTS

First, I thank the University of Missouri faculty who were part of NSEI when I entered this program: Dr. Tushar Ghosh, Dr. Sudarshan Loyalka, Dr. Mark Prelas, Dr. William Miller, and Dr. Robert Thompson. Your acceptance and support in this process has been invaluable.

I also thank the Washington University Radiation Oncology Physics faculty for allowing me the opportunity come to St. Louis to perform this research. I am and always will be honored to have worked with you all.

Thanks to Omar Wooten, Tianyu Zhao, and Hua Li for your contributions to this work.

Thank you to Dr. Lixin Ma, and Dr. S. Murty Goddu for your participation on my committee.

Finally, thanks to Dr. Eric Klein. Your support and guidance throughout this project has been invaluable. I am deeply honored to have had the privilege of working with you.

TABLE OF CONTENTS

LIST OF FIGURES

LIST OF TABLES

Table Page

LIST OF ACRONYMS/ABREVIATIONS

AAPM	American Association of Physicists in Medicine
ALL	All Fields per Fraction Delivery
BCM	Beam Current Modulation
BED	Biologically Effective Dose
BEDVH	BED-volume histogram
cEUD	Cell killing-based Equivalent Uniform Dose
CcGE	cobalt-cGy-equivalent
cGy	Centigray
CT	Computed Tomography
CTV	Clinical Target Volume
D_{97}	Minimum dose to 97% of the target volume
D_{max}	Maximum dose to a structure
D_{mean}	Mean dose to a structure
D_{min}	Minimum dose to a structure
DICOM	Digital Imaging and Communications in Medicine
DVH	Dose-Volume Histogram
EUD	Equivalent Uniform Dose
FOV	Field of View
FSS	Fields Shaping System
gEUD	Generalized Equivalent Uniform Dose

GTV	Gross Tumor Volume
HBB	Half-Beam Blocked
HU	Houndsfield Number/ CT number
ICRU	International Commission on Radiation Units and Measurements
IM	Internal Margin
IMRT	Intensity Modulated Radiation Therapy
IROC	Imaging and Radiation Oncology Core, Houston, TX
kVp	Kilovolts-Peak/CT Tube Potential
LET	Linear Energy Transfer
LQ	Linear Quadratic
mAs	Milliamp seconds/CT Tube Current
MeV	Mega-electron-volts
NP	Nominal Plan
NTCP	Normal Tissue Complication Probability
NTD	Normalized Total Dose
OAR	Organ at Risk
PDD	Percent Depth-Dose
PET	Positron Emission Tomography
PMMA	Polymethylmethacrylate
PTV	Patient Target Volume
PSPR	Proton Stopping Power Ratio
QA	Quality Assurance

RBE	Relative Biological Effectiveness
RC	Range Compensator
RF	Radio Frequency
RMW	Range Modulator Wheels
ROI	Region of Interest
RT	Radiation Therapy
SD	Standard Deviation
SF	Surviving Fraction or Single-Field per Fraction Delivery
SM	Setup Margin
SSF	Subset of Fields per Fraction Delivery
SOBP	Spread Out Bragg-Peak
SPECT	Single Photon Emission Computed Tomography
TG	Task Group
TPS	Treatment Planning System
$V_{90\%}$	Volume of the target receiving at least 90% of the prescription dose.
$V_{95\%}$	Volume of the target receiving at least 95% of the prescription dose.
$V_{98\%}$	Volume of the target receiving at least 98% of the prescription dose.
$V_{99\%}$	Volume of the target receiving at least 99% of the prescription dose.
$V_{100\%}$	Volume of the target receiving at least 100% of the prescription dose.

ABSTRACT

Purpose: A common practice in proton therapy is to plan a treatment using multiple fields, but only deliver a subset of those fields for each fraction. This practice could lead to increased uncertainty in the treatment. The aim of this study is to analyze how uncertainties impact the quality of proton therapy treatment when a rotating subset of the planned fields is delivered for each fraction rather than delivering all planned fields for every fraction.

Methods and Materials: Uncertainties were separated into two categories, physical and biological. Physical uncertainties were defined to be those that impact the location of the physical dose. Uncertainty in patient positioning is a primary example of physical uncertainty. These uncertainties were analyzed by introducing a physical uncertainty into a treatment plan and comparing resulting dose calculated for different treatment regimes. Uncertainties related to the manner in which tissue respond to radiation were considered biological uncertainties. For example, fractionation differences and the LET-dependence of proton RBE were considered biological uncertainties. These uncertainties were analyzed using models that have been proposed in the literature. Comparisons were made for different treatment regimes.

Results: Physical errors primarily impact the taget and OAR's located very near the target. Errors in a single field of a plan are partially mitigated when multiple fields are

delivered for each fraction. The effects of biological uncertainties due to differences in fractionation are very similar to the effects of hypofractionation used in radiosurgery. The caveat being that in this situation the tissue receiving hypofractionated dose is normal tissue far from the target. This results in increased biological effect in normal tissue for the same dose when fewer fields were delivered for each fraction. The LET-dependence of the proton RBE primarily impacts the target region of the patient. For parallel opposed fields the increased uniformity of the two-field per fraction treatment resulted in a RBE advantage compared to the one field per fraction treatment. The caveat being that the RBE is also dependant on tissue type (α/β). Above an α/β ratio of 4 Gy the one field per fraction treatment would result in a greater RBE advantage.

Conclusion: Uncertainty due to fractionation differences for different delivery regimes had the greatest impact on the overall treatment. Whenever possible, it is best to deliver all fields from the treatment plan in order to minimize this effect.

Chapter 1. Introduction

For proton radiotherapy treatment planning, multiple fields are used, and subsequently, each field in the treatment plan for a patient is created as if it were the only field to be delivered to the target. Because each beam or set of beams is designed to give uniform dose to the target, an option for treatment is to only deliver a subset of the beams in the treatment plan for a given fraction. An exception to this procedure occurs for targets of complicated shapes near critical structures where a single field covering the target would cause excessive dose to the critical structure. In this case, the target is covered by a set of two or more patched subfields where the distal 50% isodose line of one subfield is matched to the lateral 50% isodose line of another subfield.

The primary motivation to only deliver a subset of beams, for a given fraction, is to reduce scheduled treatment time and thus maximize the number of patients to be treated per day. However, there are several questions that arise from this practice. Is the uncertainty in each individual beam amplified by delivering only a subset of beams per fraction? If all planned beams are to be delivered, how much uncertainty is introduced by the possibility of patient migration and/or setup between beams? What radiobiological effect occurs in normal tissue when using alternating subsets of beams? These questions need to be answered in order to have confidence that the practice of delivering daily subsets of beams, according to a treatment plan, does not sacrifice target coverage or increase dose to critical organs.

1.1. Previous Related Studies.

The effect of the fractionation schedule on the quality of the treatment has been previously studied by Wang et al.[1] and Engelsman et al.[2] Wang et al.[1] evaluated the impact on interfraction variations on prostate proton therapy. The delivery scheme was only part of the study. For ten low and intermediate risk prostate patients, their results showed significant improvement over single daily beam delivery schemes for situations involving large prostate shifts perpendicular to the beam direction or femoral head rotation on the order of 15 degrees. However, these situations were rare in their study so the overall advantage of delivering both lateral beams daily was <0.6% for prostate coverage in each fraction. Also, the minimum dose to 97% of the volume of the target (D_{97}) was improved by less than 0.7cGy for all but one patient.

Engelsman et al.[2] studied the biologic effect delivering alternating subsets of fields for four different treatment sites: prostate, base of skull, lung and pancreas. They compared delivering all beams in a treatment every day to their clinical delivery scheme and single beam per day in terms of RBE-corrected absorbed dose, normalized total dose (NTD – absorbed dose corrected for fractionation effects: see Chapter 2, Section 2.3.3), and gEUD (generalized equivalent uniform dose: see Chapter 2, Section 2.3.5b). The base of skull patient group showed a significant reduction in NTD to the left frontal lobe for the delivery scheme including all beams over treating a single beam per day or the clinical protocol of rotating through six or seven unique field combinations daily. The lung patient group did not show any significant change in the NTD to the Lung-GTV

when treated with all three beams daily compared with one or two beams daily. The Pancreas patient group showed a marked decrease in the NTD to the small bowel when delivering all beams. Finally, for the prostate patient group, delivering both lateral beams every day resulted in a 30% reduction in NTD to the femoral heads. Engelsman et al.[2] also calculated the gEUD to critical normal tissues for each group. The gEUD was significantly reduced for nearly all normal tissue structures when all beams are delivered daily. Trofimov et al[3]. also compared the effect of setup variation between single beam per day and all beams per day treatment strategies for prostate cancer. They found that in the single beam per day treatment strategy, the variation in the position of the treated volume was significantly higher. The standard deviation increased on average by 25% compared with treating both beams daily.

Chapter 2. Background

Before providing answers to the questions of the previous chapter, it is necessary to first define the sources of uncertainties, and to discuss the importance of these uncertainties in proton radiation therapy treatment. It is also relevant to know the current methodologies for analyzing and mitigating these uncertainties, and to know the capabilities and limitations of the treatment planning system.

2.1. Beam Delivery.

Proton therapy treatment systems vary greatly. However, each of them can be divided into three subsystems: the accelerator, the beam transport system and the treatment head. The accelerator provides the energy to the protons. The beam transport system extracts the high energy protons and transfers them to the treatment room while the treatment head shapes the beam into its final form that is delivered to the patient. With each of these subsystems, there is an associated contribution to the physical uncertainty in the delivered proton beam.

2.1.1. Proton Accelerators and Beam Transport Systems.

Current methods for accelerating clinical protons to therapeutically useful energies (60-250 MeV) fall under two main categories: cyclotrons or synchrotrons. Each has its own set of benefits and limitations. The primary benefit of a synchrotron

accelerator is that the energy of the proton beam can be selected at the accelerator. The proton beam from a cyclotron is always extracted at the same energy. However, a cyclotron can be made much smaller than a synchrotron for the same maximum proton energy.

2.1.1a. Cyclotrons.

Originally developed by E. O. Lawrence in 1932[4], a cyclotron consists of semicircular shells called "dees" placed within a uniform magnetic field (Figure 2.1). Protons injected into the center of the space between the "dees" are accelerated toward the negatively charged dee. Once the protons enter the space within the dee the electrostatic force is no longer acting upon it. The only force on the proton is the Lorentz force from the magnetic field causing the protons to follow a circular path until they reach the gap between the "dees". If at this point the polarity of the potential between the "dees" is reversed the protons are given additional kinetic energy as they pass through the gap. The radius of the circular path of the protons within the magnetic field increases with increasing kinetic energy of the protons. If this process is repeated many times the protons will follow a spiral path outward from the center of the "dees" increasing in kinetic energy every time they pass through the gap. This is the fundamental principle behind the operation of a cyclotron.

Lawrence's original cyclotron used a uniform magnetic field and a constant frequency of oscillation in the polarity of the "dees". This design is insufficient to produce protons of therapeutic energies. As the kinetic energy of the protons increases, corrections must be made to account for relativistic effects on the mass of the protons[5].

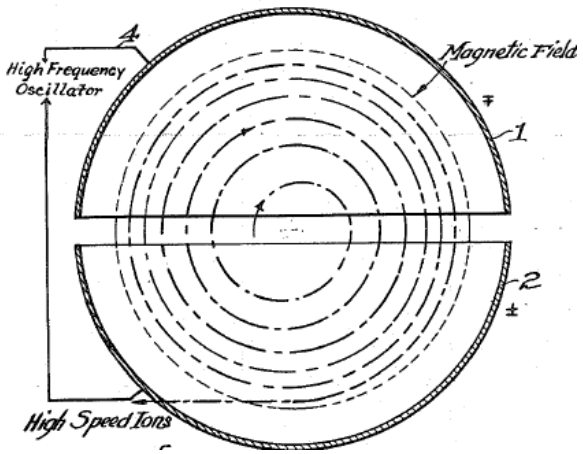

Figure 2.1. A diagram reproduced from the Lawrence's patent[4] showing the path of protons withing the "dees" of a cyclotron. Acceleration occurs in the space between the "dees". For protons the magnetic field would be directed out of the page[4].

There are two ways to compensate for relativistic effects in a cyclotron. The first option is to spatially vary the magnetic field so that it increases in strength as the protons move away from the center. In this way the angular frequency of the protons can be held constant so the oscillation in polarity of the "dees" can remain at a constant frequency[6]. This design of a cyclotron is also referred to an isochronous cyclotron. An advantage of this design is that it can produce a continuous beam. The accelerating potential frequency in an isochronous cyclotron is constant. Therefore, protons can be constantly fed into the cyclotron and the accelerating potential frequency is the always optimal for accelerating them.

The other method of accounting for relativistic effects in a cyclotron is to lower the frequency of oscillation in the dee potential to match the frequency of orbiting protons. This design is referred to as a synchro-cyclotron[5]. This design is less complicated from a technical standpoint. The only modification that has to be made to the original cyclotron design is to change the high frequency circuit connected to the

"dees" to produce a time varying frequency. However, the time varying frequency of the accelerating potential in synchro-cyclotrons requires the beam be pulsed at a frequency equal to that rate at which the accelerating potential changes.

2.1.1b. Synchrotrons.

Synchrotrons can also be used to accelerate protons to therapeutic energies. A synchrotron consists of an alternating arrangement of accelerating elements, focusing elements, and bending magnets setup in a ring (Figure 2.2). The operation of a synchrotron is very similar to the operation of a synchro-cyclotron. As the kinetic energy of the protons is increased the frequency of the RF signal applied to the accelerating elements is adjusted to account for relativistic effects. However, unlike the cyclotron where the proton path is dependent on the energy of the particle, a synchrotron only has one possible beam path. Therefore as the energy of the protons increase the strength of the magnetic field in the bending magnets is also increased in order to keep the protons following the same path[5].

An advantage of using a synchrotron is that the energy of the protons extracted from the accelerator is user selectable. In a cyclotron, protons have to be accelerated to a specified energy in order to contact the beam extraction apparatus. In a synchrotron, the path of the protons is forced to be independent of the kinetic energy so they can be extracted once they reach the desired energy.

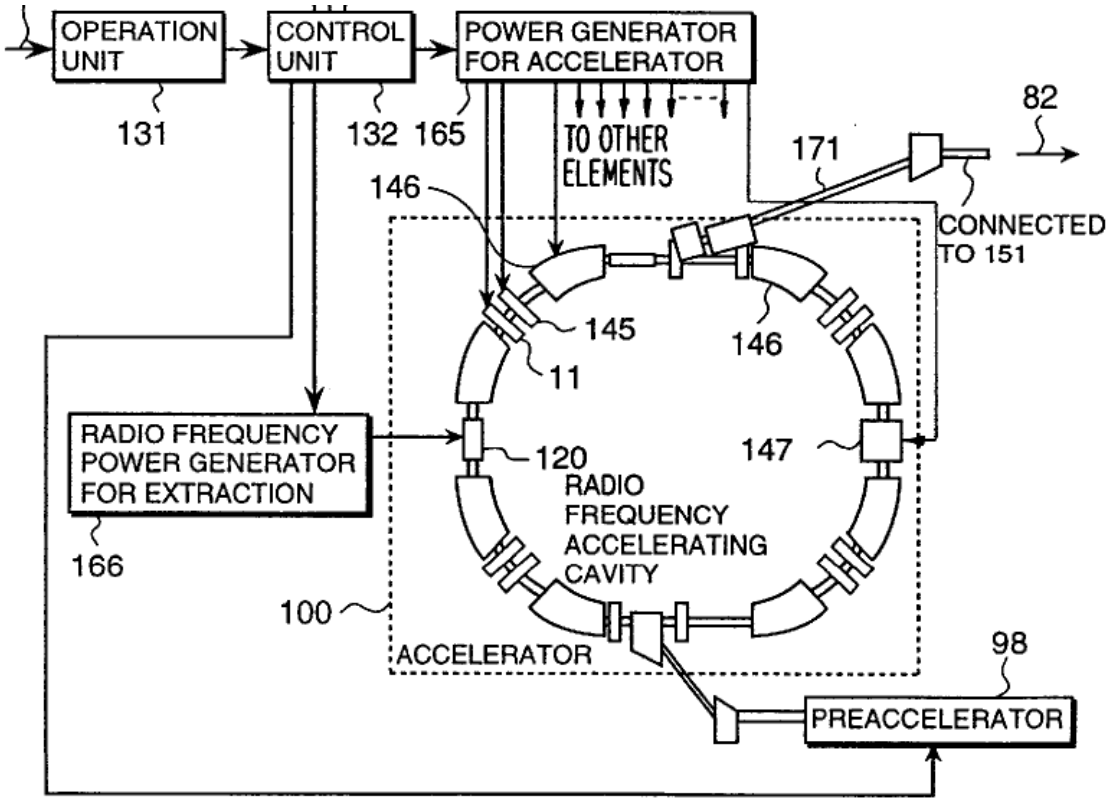

Figure 2.2. A diagram illustrating the operation of a synchrotron[7].

2.1.1c. Beam Transport System.

Except for the MEVION system (described later, in section 2.1.3), the proton accelerators for all treatment facilities are located outside the treatment vault, and the proton beam is transferred from the accelerator to the patient via the beam transport system. Historically, this method has been used for two reasons. First, accelerators are too large to fit in the treatment vault. More importantly, the financial cost of accelerators has made it more cost effective to utilize a single accelerator to provide a proton beam to several treatment rooms rather than unique accelerators for each treatment room. The

bending magnets used to switch the beam path from room to room are cheaper than having a unique accelerator for each treatment vault[8].

The beam transport system consists of an evacuated channel connecting the extraction port on the accelerator to the exit window in the treatment head. Bending magnets and focusing coils and beam monitoring detectors are placed along the channel to keep the proton beam as centered and narrow as possible as travels through the channel. Since the cyclotron is attached to the gantry in the MEVION system, the beam transport system is greatly simplified[8].

For facilities the use cyclotrons to accelerate protons, the beam transport line may also contain the energy selection system. The energy of the protons leaving a cyclotron is predetermined by the design of the accelerator, and the maximum energy of the proton beam. Lower energy beams are achieved by placing material in the beam path to reduce the proton energy.

2.1.2. Treatment Head.

The proton beam exiting the beam transport system is very narrow and essentially monoenergetic. It is the function of the treatment head to modify this beam to achieve therapeutic useful dose distributions in the patient. There are two major methods of by which treatment heads achieve these results; passive scattering and spot scanning. Passive scattering uniformly spreads the narrow beam laterally and in depth to create a volume of uniform dose in the patient where the distal extent of the uniform volume matches the distal extent of the target plus margins. Spot scanning modifies the energy

and lateral direction of the narrow beam to build a uniform dose distribution around the target from the contributions of the bragg-peaks of many closely spaced small beams.

The design of the treatment heads for passive scattering and spot scanning are quite different. The proceeding subsections provide a generic description of the function of the components the beam passes through from the exit widow to the patient.

2.1.2a. Passive Scattering.

Figure 2.3 shows from left to right the sequence of components of a passive scattering treatment head in the order the proton beam passes through them. If the energy selection system is not a part of the accelerator design or the beam transport system, the first component the beam passes through is a lead scatterer. This spreads the beam, laterally. It is at this point that the beam passes through the range modulator to create a spread out bragg peak (SOBP). A common form of range modulator is the modulating wheel. This is a wheel that rotates in the beam with areas of different thicknesses of material. For each section of the wheel the range of the beam is modified. To get a uniform SOBP the constituent bragg peaks with a deeper range must be given more weight than shallower peaks because the dose at the proximal edge of the SOBP is the sum of the dose from that bragg peak plus the entrance dose of all the bragg peaks with deeper range. This weighting of the individual bragg peaks is accomplished by weighting the angular width of the different sections of the modulator wheel, known as beam current modulation (BCM). The beam then passes through a primary absorber which sets the maximum range of the beam.

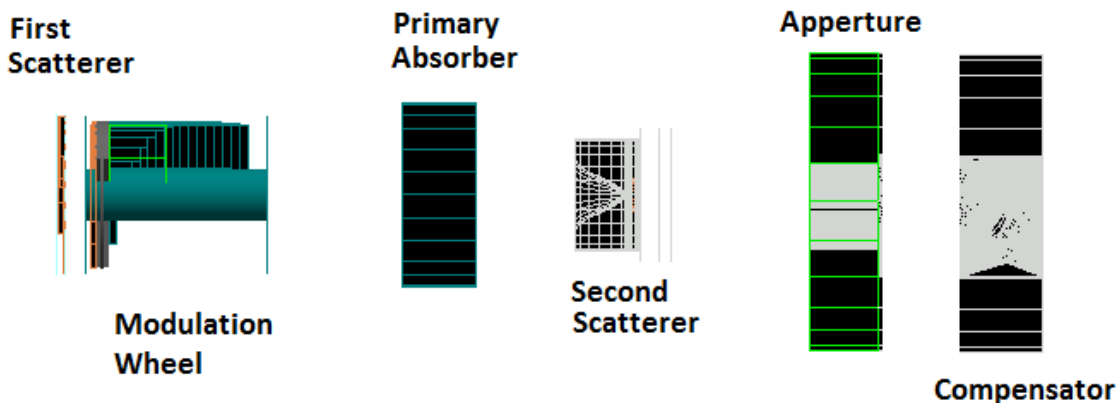

Figure 2.3. Diagram illustrating the parts of a passive scattering treatment head.

After passing through the first scatterer, modulation wheel, and primary absorber the beam is spread out but since higher energy protons are scattered less than lower energy protons there is a spatial distribution of energy is the beam this is corrected by the second scattering filter. This filter is made of high-Z material surrounding a low-Z material in the central part of the beam. The low-Z material degrades the energy of the protons with less scattering than high-Z material. Because the proton energy increases toward the central part of the beam the second scattering filter is contoured so that the central part of the beam has more material than the edges of the beam to create a broad flat beam.

Once a broad flat beam is achieved it can be tailored to match the target. The aperture and compensator perform this task (Figure 2.3). The lateral extent of the beam reaching the patient is defined by the aperture, a brass plate cut to the shape of the target. The compensator is a machined plastic absorber placed in the beam path. In regions where the beam needs to reach deeper in the patient to treat the distal portion of the target, the amount of plastic in the compensator is reduced. In places where the distal depth of the target is shallower, the plastic is thicker. The combination of the aperture

and compensator produces a dose distribution in the patient that matches the lateral and distal extent of the target. An unavoidable result of passive scattering is that normal tissue proximal to the target will receive some spill over of prescription dose due to the range modulation being spatially uniform in the beam.

2.1.2b. Spot Scanning.

Figure 2.4 shows from left to right the sequence of components of a spot-scanning treatment head in the order the proton beam passes through them. In a spot scanning treatment head, the scattering filters, aperture, and compensator are replaced by two pairs of bending magnets, one pair for the x-direction and one for the y-direction. The function of the range modulating wheel is unnecessary for spot scanning. In spot scanning, the dose is delivered in layers situated in the distal to proximal direction. After the dose is delivered to a distal layer of the target, the beam range is reduced by reducing the energy of the proton beam and dose is delivered to the next proximal layer of the target. Because the lateral extent of the delivered dose can easily be modified by changing the maximum magnetic field strength of the scanning magnets from layer to layer, it is possible to deliver a plan using spot scanning that is more conformal than with passive scattering.

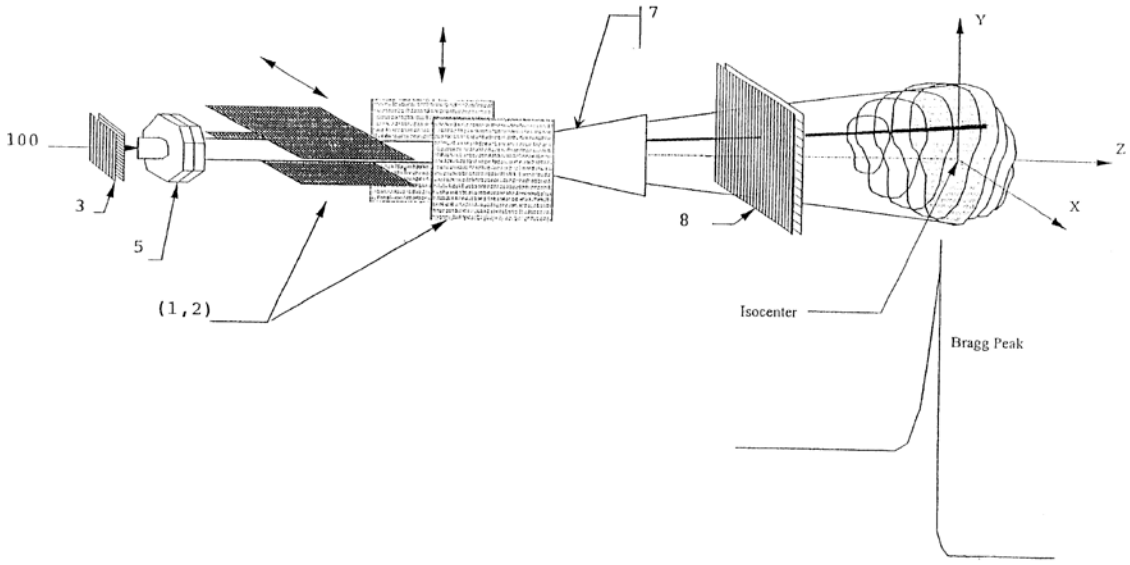

Figure 2.4. Diagram of a spot-scanning treatment head[9].

2.1.3. The MEVION System.

The proton therapy system used at Barnes-Jewish Hospital is from MEVION Medical Systems. The MEVION proton therapy delivery system (Figure 2.5) differs from other proton therapy systems in several ways. First, the MEVION system is a single room system. In other proton therapy facilities, several treatment rooms are supplied by a single accelerator through a complicated beam transport system. The 10 Tesla synchro-cyclotron in the MEVION system, is mounted on the gantry with the exit

port directed toward the patient so the beam transport system essentially removed.

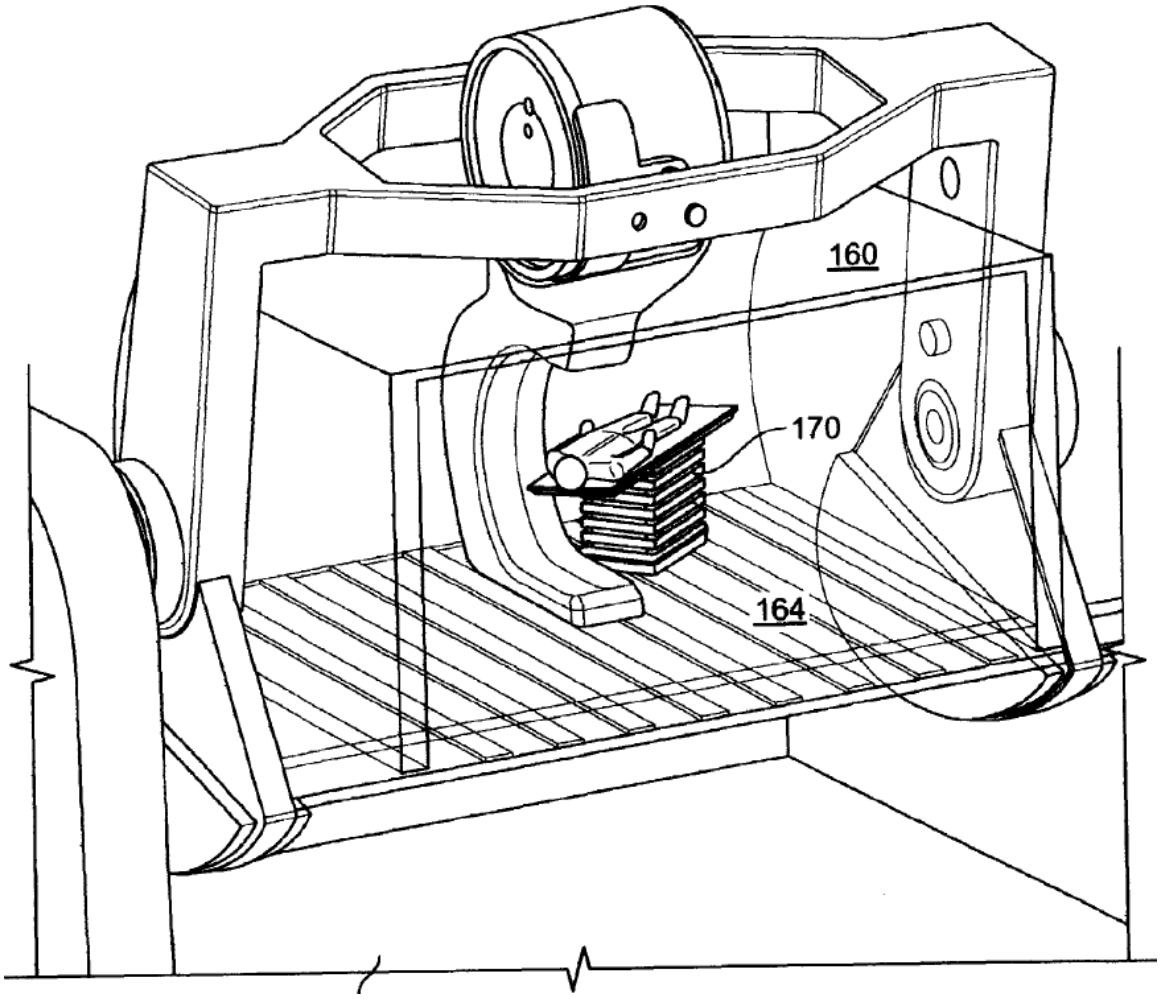

Figure 2.5. A cut-away representation of a MEVION treatment vault[6].

Another difference between the MEVION system and other proton facilities is the gantry. Rather than using a gantry that rotates 360 degrees around the patient similar to conventional radiation therapy gantries, the MEVION gantry rotates 190 degrees from vertical up to vertical down. A 6-D robotic couch provides the necessary freedom in patient positioning to allow for any beam trajectory.

2.2. Physical Uncertainties.

The term physical uncertainties is meant to describe any deviation in the dose delivered that is created by uncertainty in the material or geometric properties of the proton beam and any component the beam passes through from the injection at the accelerator to the distal range in the patient.

2.2.1. Delivery System Uncertainties.

Uncertainty in the range of proton beams comes from several different sources. Uncertainty in the thickness of beam modifying devices in the accelerator (range modifier, compensator, scattering system components) combine to give, according to Moyers et al.[10], 3mm of uncertainty in the range of the proton beam in tissue.

Two fundamental contributors to the range uncertainty of proton beams stem from uncertainty in the energy of the proton beam itself and uncertainty in the energy deposition of the incident protons as they pass through matter.

It is not possible to produce a proton beam that is truly monoenergetic when it exits the cyclotron. The vacuum in the acceleration chamber is not perfect so there will be a small amount of interactions between the protons and the medium. There is a special distribution of the protons within each pulse so they will not all see the exact same pulse from the RF signal for the exact same amount of time. Also, the exit port on the accelerator has a finite radial size. Since there is a relationship between the energy of the protons and the radial position, there will be an energy distribution introduced there as well. Uncertainty in the beam energy is further increased by the field shaping system

(FSS). Manufacturing tolerances of the parts of the FSS will contribute to a small increase in the energy distribution of the proton beam.

2.2.2. CT (Hounsfield) Number (HU) Conversion to Proton Stopping Power Ratio (PSPR) Uncertainties.

Another source of uncertainty in range is in the CT (Hounsfield) number (HU) conversion to proton stopping power ratio (PSPR) in tissue. The current method of calibrating HU to PSPR was proposed by Schneider et al.[11] and verified by Shaffner and Pedroni[12]. The starting point for this calibration is to define the scaled Hounsfield unit (HU_{sc}). The CT number read from the CT scanner gives a value of -1000 for air, 1 for water, and 1000 for bone. The scaled Hounsfield unit moves this scale to 0 for air, 1000 for water, and 2000 for bone. Schaffner and Pedroni[12] define HU_{sc} as:

$$HU_{sc} = HU + 1000. \tag{1}$$

Schneider et al.[11] defines HU_{sc} as:

$$HU_{sc} = 1000\frac{\mu}{\mu_w} \tag{2}$$

where $\frac{\mu}{\mu_w}$ is the ratio of the linear attenuation coefficient of tissue to the linear attenuation coefficient of water.

Equation 2 can be derived from equation 1 by substituting the definition of the HU

$$HU = 1000\left(\frac{\mu}{\mu_w} - 1\right) \tag{3}$$

into equation 1 and simplifying. From this definition it is clear that the HU_{sc} depends on both the material properties of the tissue and the energy spectrum of the scanner.

The material properties that most influence the HU_{sc} are the relative electron density and the effective atomic number of the tissue. The relationship between these properties is defined by Schaffner and Pedroni[12] with the equation:

$$HU_{sc} = \rho_e^{rel}\left(A\tilde{Z}^{3.62} + B\hat{Z}^{1.86} + C\right) \tag{4}$$

where ρ_e^{rel} is the electron density of the scanned material relative to water. $\tilde{Z}$ and $\hat{Z}$ are definded by Schneider et al.[11] to be

$$\tilde{Z} = \left[\sum \lambda_i Z_i^{3.62}\right]^{1/3.62}, \tag{5}$$

$$\hat{Z} = \left[\sum \lambda_i Z_i^{1.86}\right]^{1/1.86}, \tag{6}$$

Where λ_i is the is the number fraction of the of ith component of the material being scanned. The constants A, B, and C can be found empirically from multiple linear fits of measured HU_{sc} data of materials of known composition to equation 4.

For the same materials the PSPR can be calculated using an approximation of the Bethe-Bloch formula

$$PSPR = \frac{\rho_e^{rel}\{\log[2m_e c^2\beta^2/I^t(1-\beta^2)]-\beta^2\}}{\{\log[2m_e c^2\beta^2/I^w(1-\beta^2)]-\beta^2\}}. \tag{7}$$

Where I^t and I^w are the mean ionization potential of tissue and water respectively.

The HU to PSPR calibration curve is found by plotting the HU_{sc}, calculated by equation 4, versus the PSPR, calculated by equation 7 for several reference tissues with well defined elemental composition. This plot can be broken into sections based on tissue type. In each section, the data points can be fit with a straight line. Schneider et al.[11] use the following tissue categories: lung ($0<HU_{sc}<850$), adipose tissue ($930<HU_{sc}<1023$), organs and muscle ($1023<HU_{sc}<1060$), and bone ($HU_{sc}>1060$). For HU_{sc} values between the lung and adipose tissue there is a region assumed to be a linear transition between the two tissue types.

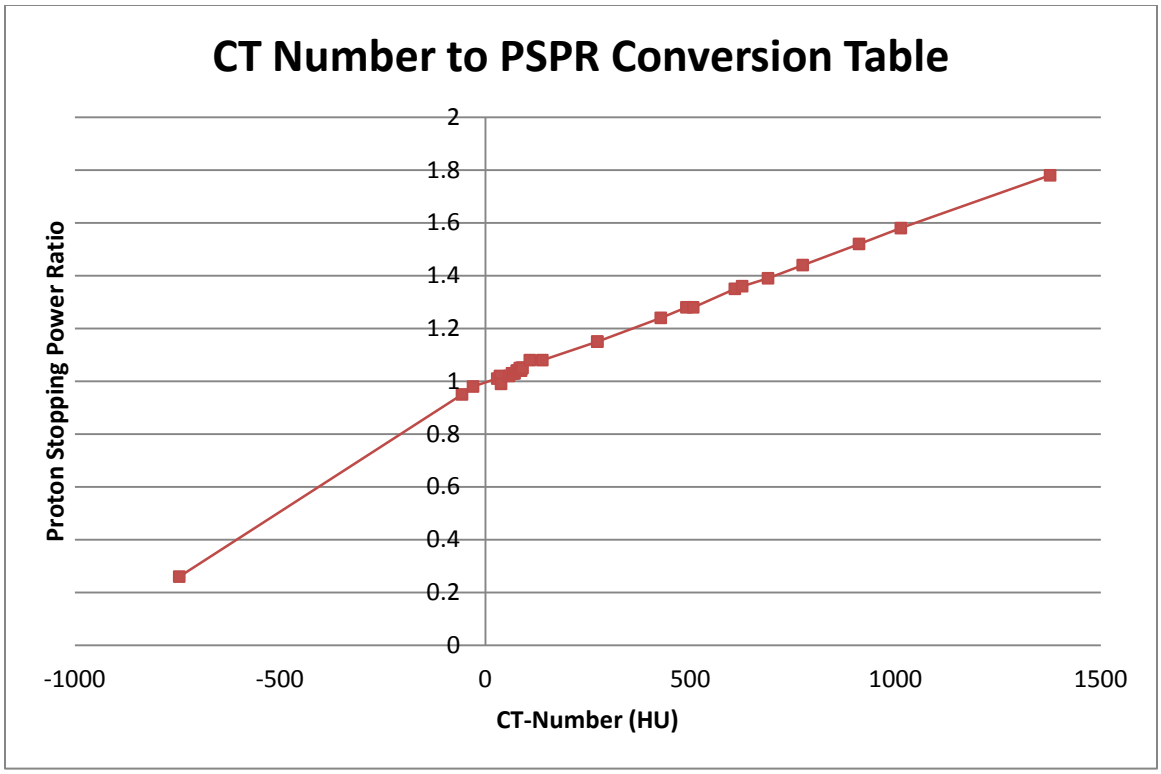

Figure 2.6. An example of an HU to relative proton stopping power ratio conversion created using the methods of Schneider et al.[11]

The exact value of the transition between tissue types may be different for different scanners depending on the energy spectrum of the CT scanner. Figure 2.6 shows an example of the conversion table created for clinical use at Barnes-Jewish Hospital in St. Louis.. Schaffner and Pedroni[12] determined the transition points on the calibration curve by creating an histogram of the number of voxels vs. the HU_{sc} for several sites in the human body. The width of the peaks in the CT histogram gives an idea of region over which each tissue type resides.

Schneider et al.[11] verified this calibration by comparing it with the stopping power measured with proton radiography of a sheep head. The sheep head was irradiated with a 219 MeV proton beam the residual range of the exiting protons were measured to

produce a 2-dimensional map of the effective stopping power. This was compared to a 2-dimensional map of stopping powers created by integrating the stopping power calculated from the HU to stopping power calibration over the proton beam path in a CT of the same sheep head. They found that the CT calibration matched the measured stopping power with a standard deviation of 1.4% with a maximum deviation of 8.9%. The CT calibration differed from the measured stopping power ratio by more than 3% in 4.7% of the pixels of the CT calibration.

Schaffner and Pedroni[12] analyzed the precision of this conversion by comparing the value taken from the calibration to the measured stopping power ratio of several homogenous tissue samples. They found that the CT conversion matched the measured stopping power to with one percent for all tissues. They estimate that error in the CT calibration and CT scan translates to an error in proton range of 1.8% in bone and 1.1% in soft tissue.

2.2.3. Proximal and Distal Margins.

Moyers et al.[10] suggests that the magnitude of uncertainties is approximately 3.5% of nominal proton range in tissue due to the uncertainty in the proton stopping power ratio in addition to the 3mm uncertainty from beam modifying devices in the accelerator (range modifier, compensator, scattering system components). Range uncertainty applies to both the distal and proximal extent of the target and result in suggested distal and proximal margins of:

- $distal\ margin = (0.035 \cdot most\ distal\ depth\ of\ target) + 3mm,$ (8)
- $proximal\ margin = (0.035 \cdot most\ proximal\ depth\ of\ target) + 3mm.$ (9)

Andreo[13] highlighted the need to include margins to account for an uncertainty in the range of proton and heavier charged particle. He showed, using Monte-Carlo simulations, that the uncertainty in the mean excitation energy of tissue, and water, leads to a fundamental uncertainty in the range of proton beams in water.

Park et al.[14] uses the same margins as Moyers et al.[10] to define a beam-specific PTV which is a label applied to the target region defined by Moyers et al.[10] for each beam. While useful for specifying that margins are created for each beam in the treatment plan, a beam-specific PTV is not useful for reporting or recording target coverage since for each beam, the planned treatment volume is different. However, ICRU 78[15], recommends creating a PTV based solely on the lateral uncertainties for the purpose of recording and reporting the target dose.

Sejpal et al.[16] described the use of these margins for proton prostate planning. They demonstrated that for ten patients in their study, the margins are sufficient to provide no clinically significant deviation in dose delivered to the target. They simulated rotational setup errors of up to three degrees of couch rotation and up to 5 degrees of patient roll.

Beltran et al.[17] studied the dosimetric impact of rotational setup errors in photon IMRT treatments of pediatric brain tumors in the posterior fossa in terms of the generalized equivalent uniform dose (gEUD), or the uniform dose distribution over a region of interest (ROI) that has the same biological effect as the heterogeneous dose distribution that is delivered. The details concerning how gEUD is calculated will be discussed in a later section. They found that the rotational setup errors of up to 2 degrees yielded negligible consequences (<2%) in the gEUD compared to unrotated setup. For a

4 degree rotational setup error they found that the gEUD of serial type normal tissue by 10% and the gEUD for the PTV changed by 5%. They state that these results may not be applicable to protons, but based on Sejpal's work[16], given sufficient margins and smearing, the dosimetric effect on the PTV will be small.

Trofimov et al.[3] studied the effect of interfractional variation of soft tissue and pelvic boney anatomy on proton therapy delivery for prostate patients, particularly the positions of the distal and proximal 98% isodose lines. Proton treatment plans were created for 10 patients treated with photon IMRT. During treatment, between 21 and 43 computed tomography (CT) scans were acquired for each patient. In the CT scans taken during treatment, measurements of subcutaneous adipose tissue, and distance to the distal surface of the target, and the rotation angle of the femoral heads were taken. The proton treatment plans were then applied to the treatment CT scans and analyzed for coverage of the prostate. They found that in most cases, smearing of the compensator, or matching any given region of the range compensator (RC) to the largest water equivalent depth of the target within that region, was sufficient to account for the variations observed in setup.

Vargas et al.[18] also studied the effect of prostate positional variation in proton therapy. Their study used different beam geometries. Rather than delivering treatment with two opposing lateral beams, they treated with two beams pitched from 4 to 12 degrees posterior to lateral. Margins and smearing were comparable to margins suggested by Moyers. For each of the 10 patients, 11 additional plans were created. Four plans included a 5mm shift in the anterior, posterior, superior, or inferior direction. Three

plans included a 10mm shift in the posterior, superior, or inferior direction. The other four plans included the following combination of three 10mm shifts:

1. Superior, posterior, and left.
2. Superior, anterior, and right.
3. Inferior, posterior, and right.
4. Inferior anterior, and left.

With shifts <5mm, no clinically significant change in the prostate coverage was seen. Significant loss of coverage was seen for shifts ≥10mm.

2.2.4. Geometric Uncertainties and Lateral Margins.

In this writing, geometric uncertainties are defined appropriately by van Herk et al.[19] Systematic uncertainties stem from treatment planning, patient simulation, and machine calibration. These uncertainties affect all fractions in the same manner throughout treatment. Random geometric uncertainties rise from variations in the position of the target and critical organs relative to the proton beam. These uncertainties include translational and rotational setup errors, intrafractional target motion, and interfractional target variation due to anatomical changes during and between fractions (deformation, position, etc.). While random uncertainties exist throughout treatment, the magnitude of the deviations caused by random uncertainty will vary fraction to fraction.

Van Herk et al.[19] studied the physical and biological effect of translational random geometric errors on dose distributions using photon beams. They found that the random errors can be modeled by a Gaussian blurring of the dose distribution. In effect, random translational errors create a widening of the penumbra region in the total dose

distribution including all fractions. A limitation of that study is that rotational setup errors, heterogeneities, target deformation, and systematic errors, were all ignored. However, their results can be applied to the lateral edges of a proton field under the same conditions since in the lateral direction photons and protons behave in a similar manner.

With the exception of interfractional target motion and deformation, geometric uncertainties are compensated for in treatment planning through the use of lateral margins and "smearing" of the RC. Moyers[10] suggests the following:

$$Lateral\ margin\ around\ CTV = IM + SM + (90 - 50\%\ penumbra) \qquad (10)$$

- Where IM is the internal margin accounting for target motion (magnitude depends on the location of the target.
- SM is the setup margin accounting for how closely the therapists are able to align the patient with the beam (about 5mm).
- The 90-50% penumbra is the distance between the 90% and the 50% isodose lines at the most lateral edge of the field whereby the magnitude depends on depth since the penumbra of proton beams increase with depth.

Urie et al.[20] suggested a method of mitigating the effect of lateral setup errors on the distal edge of the beam called "smearing" the RC. A small beam misalignment with the RC directly to the shape of the distal edge of the target would result in an underdose to the target with concurrent overdose to structures distal to the target. Matching any given region of the RC to the largest water equivalent depth of the target within that region increases the dose distal to the target while maintaining target coverage for small beam misalignments. Moyers et al.[10] suggests smearing to be defined as;

$$smearing = [(IM + SM)^2 + 0.03 \cdot (distal\ CTV\ depth + compensator\ thickness)^2]^{0.5}. \quad (11)$$

This methodology is used for setting up the lateral margins and smearing in our particular clinic.

2.2.5. Patient Migration.

A limitation of the treatment planning margins discussed in previous sections is that they are based on the assumption that the patient is stationary during treatment. It is assumed that patient immobilization devices sufficiently limit patient motion to the degree that the uncertainty introduced is small compared to other uncertainties in the treatment plan.

Engelsman et al.[21] analyzed intrafraction motion for several different immobilization devices used at the Northeast Proton Therapy Center. As part of their treatment procedure, two orthogonal x-ray images are initially taken of the patient for setup. Prior to delivery of each treatment field another set of images were taken to verify the patient position. The difference between this verification image and the initial setup images is the intrafractional patient motion. They found that the average total displacement was 1.3 mm for patients using immobilization devices that were rigidly connected to the treatment couch. For patients using immobilization devices that were not rigidly connected to the treatment couch, the average total displacement was 1.9 mm.

They also calculated distance within which the patients would remain with a 95% probability. The average value for this distance was 3mm for rigidly connected devices and 4.7mm for devices not rigidly connected. These values indicate that for

immobilization devices that are rigidly connected to the treatment table, verification of the patient position between beams may not be necessary if the initial setup accuracy is sufficiently high.

These result assumed that the delivered fields were coplanar, and that no couch rotation or larger translation occurred between setup and the treatment field delivery. Engelsman et al.[21] found that couch rotations between the setup field and treatment field greater than 40 degrees had a total displacement twice as large as unrotated patients.

2.2.6. Calculation Uncertainty.

Another source of uncertainty in proton range stems from the dose calculation algorithms for most commercial treatment planning systems, specifically the way in which they inhomogeneities are handled. Hong et al.[22] developed an algorithm that is the basis of dose calculations of current commercial proton treatment planning systems. Their dose calculation algorithm calculates dose through convolution of pencil-beams. The central depth dose of each pencil-beam is calculated from the water equivalent depth along the beam path. The lateral profile of each pencil-beam is modeled by a Gaussian fit and accounts for small angle multiple Coulomb scattering of the protons. The major drawback of this algorithm is that it less accurate when accounting for the geometry of heterogeneities in the beam path[23]. Also, the pencil-beam algorithm is based on measurements (or Monte-Carlo calculations) of depth-dose profiles in water for which the contribution of inelastic interactions in tissue are not well modeled due to the presence of other elements with differing interaction cross-sections.

Dose calculation algorithms that use Monte-Carlo simulations rather than convolving pencil-beams are considered to be quite accurate. However, Monte-Carlo dose calculation algorithms have their own set of drawbacks. Specifically, they are currently too time-consuming to make them clinically viable.

2.3. Radiation Biology.

In analyzing whether "subset of the day" proton treatment strategies are more or less effective than treatment strategies including all beams, much of the difference in treatment strategies lies in the biological effect of the treatment strategies. In this section, the radiobiological parameters used to compare treatment strategies along with how they might be used to compare different treatment strategies are defined.

2.3.1. Proton RBE (Relative Biological Effectiveness).

Relative biological effectiveness (RBE) is a measure of how much dose from a proton beam is required to have the same effect on a biological system as one that is irradiated by photons from a ^{60}Co photon beam under identical conditions[15]. It is given by:

$$RBE = \frac{D_{photon}(effect)}{D_{proton}(effect)}. \quad (12)$$

The ICRU 78 report[15] recommends a value of 1.1 to be used for the RBE of proton beams. This value is based on an average value found from studies of in vitro and in vivo studies of cells. The In vitro studies compiled in ICRU 78[15] and Pagenetti[24] showed a mean RBE value of 1.19. The cell types in the in vitro studies were divided into 2 categories, V79 cell and non-V79 cells. The V79 cells showed a greater RBE

(1.24) than non-V79 cells (1.12). In vivo studies showed a lower value for RBE than in vitro studies. The mean RBE value from in vivo studies[15, 24] was 1.1.

The ICRU 78[15] report contains no determination of RBE for human tissues. All of the determinations of proton RBE in the ICRU 78 report were from animal studies. Clinical experience has, however, indicated that an RBE value of 1.1 is reasonable for human tissues and is currently adopted by clinical trial groups[15].

The ICRU 78[15] report cited several studies that showed an increase in RBE of 5-10% at the distal end of a spread-out Bragg peak (SOBP). The result of this increase is to extend the range of the RBE-weighted dose by 1-2mm. Their recommendation is that this should be considered in treatment planning when organs at risk (OARs) are located distal to the target.

However, the recommendation for the continued use of 1.1 for the RBE is largely based on Paganetti et al.[24] Their rationale at the time for continued use of the generic RBE value was that uncertainty in RBE determinations for human tissues was too great and clinical experience did not contraindicate its continued use. Paganetti et al.[24] stressed the need for further study of RBE values and normal tissue reactions.

While ICRU 78 recommends the use of the generic value of 1.1 for the RBE associated with proton beams, the RBE of proton beams is not that simple. Linear energy transfer (LET), track structure, dose, endpoint, and tissue type all affect RBE[25].

Paganetti and Schmitz[26] demonstrated that the modulation technique used to deliver a proton beam also plays a role in the RBE. They found that as the initial energy of the proton beam increased, the magnitude of increase in RBE at the distal edge of the SOBP decreased in CH2B2 Chinese hamster cells. These results were based on

simulations using PTRAN (a Monte-Carlo environment) to calculate absorbed dose and energy distributions, and a microdosimetric response function model or a track distribution model to calculate RBE.

Their model also neglected neutrons and secondary charged particle because PTRAN did not have the capability of tracking them. The rationale for this being acceptable was that in the Bragg peak region secondary charged particles only contributed 1-2% to dose. For neutrons, measurements made with a 175 MeV at COSY (Cooler Synchrotron, Julich) showed negligible contribution to biological dose in the SOBP[26].

It can be shown that the RBE versus physical dose relationship leads to a maximum and minimum value for RBE[27-29]. Starting from the linear quadratic (LQ) model for equal surviving fractions the following relation holds

$$\alpha_{photons}d_{photons} + \beta_{photons}d_{photons}^2 = \alpha_{protons}d_{protons} + \beta_{protons}d_{protons}^2. \quad (13)$$

where α and β are the linear and quadratic coefficients of radiation damage respectively, and d is the physical dose. The subscripts indicate the radiation source.

As physical dose for both modalities goes to zero, the quadratic terms of equation 13 can be neglected yielding

$$\alpha_{photons}d_{photons} = \alpha_{protons}d_{protons}. \quad (14)$$

Combining equation 12 and equation 14 yields

$$RBE = \frac{\alpha_{proton}}{\alpha_{photon}}. \quad (15)$$

This quantity is defined asRBE_{max}.

As dose approaches infinity in equation 13 the linear terms can be neglected leading to a minimum value for RBE

$$RBE_{min} = \sqrt{\frac{\beta_{proton}}{\beta_{photon}}}. \quad (16)$$

Carabe-Fernandez and Dale[27, 28] showed that, using the maximum and minimum RBE, the alpha-beta ratio of tissue for photons, and the physical dose, RBE can be expressed as

$$RBE = \frac{-(\alpha/\beta)_{photon} + \sqrt{(\alpha/\beta)^2_{photon} + 4d_{proton}\left[(\alpha/\beta)_{photon} RBE_{max} + RBE^2_{min} d_{proton}\right]}}{2d_{proton}}. \quad (17)$$

This RBE model results in and RBE-corrected dose as shown in Figure 2.7.

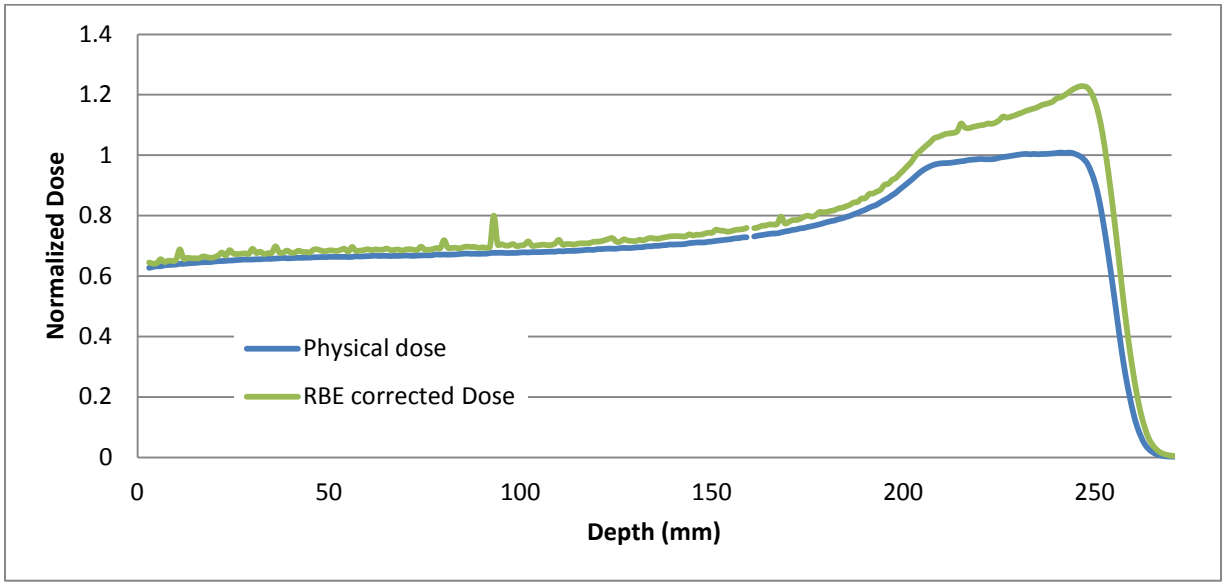

Figure 2.7. Lower Curve (Blue): the physical dose for an SOBP with range of 25 cm and modulation of 5 cm. Upper Curve (Green): the LET-dependant, RBE-corrected dose calculated from the same SOBP.

2.3.2. Biological Effective Dose (BED).

A basic explanation of the concept and use of biological effective dose (BED) can be found in Jones et al.[30] BED is used to characterize the biological effect the

fractionation and total dose has for a given treatment protocol. For photons, it is given by the equation:

$$BED = nd\left[1 + \frac{d}{(\alpha/\beta)}\right]. \quad (18)$$

- *n* is the number of fractions in the treatment.
- *d* is the physical dose per fraction
- α/β describes the radiosensitivity of the tissue of interest.

For high-LET radiations, equation 18 must be augmented to include the RBE of the particle beam. Carabe-Fernandez et al.[27] showed that the BED for high-LET particle beams, when RBE is included, should follow:

$$BED_H = n_H d_H\left[RBE_{max} + RBE_{min}^2 \frac{d_H}{(\alpha/\beta)_L}\right]. \quad (19)$$

Where the subscript, *H*, relates to the high-LET beam, *L*, relates to a photon beam, and $RBE_{max/min}$ are the maximum and minimum RBE defined previously. Substituting the RBE value of 1.1 into equation 19 gives:

$$BED_H = n_H(1.1d_H)\left[1 + \frac{(1.1d_H)}{(\alpha/\beta)_L}\right]. \quad (20)$$

Given two treatment plans with differing total physical dose and number of fractions, they are equivalent if the BED calculated for one plan is equal to the BED of the other.

The importance of BED in proton therapy for analyzing the difference between delivering all beams daily and treating a rotating subset of beams daily is concerned with the entrance portion of the proton beams. For a treatment including a rotating subset of beams, the dose per fraction in the entrance region of the beam will be greater than for treatments including all beams. However, the total physical dose delivered is the same

for either treatment plan. Using equation 20, it is clear that the BED to normal tissue in the entrance region of the proton beams will be higher for the rotating subset of beams than for all beams.

A drawback of BED is that time between fractions is not included in the model. For proton treatments with a rotating subset of daily beams the BED in the entrance region of the beam is increased. However, it is likely that the time between the delivery of any particular beam is prolonged allowing for more time for repair and repopulation to take place.

2.3.3. Normalized Total Dose (NTD).

Normalized Total Dose (NTD) quantifies the biological effect of a given radiation treatment strategy by equating the BED of that treatment strategy to the BED of a standard treatment strategy. The standard treatment strategy that is usually used is for calculating NTD is photon treatment in fractions of 2Gy each. The definition of NTD is the physical dose given with the standard fractionation schedule that gives the same biological effect as the nonstandard treatment strategy.

An advantage of using of NTD rather than BED alone for quantifying the biological effect of a treatment strategy is that BED can be described as the dose given in an infinite number infinitely small fractions gives the same effect as the fractionation schedule being tested. This quantity does not match clinical experience. By relating the biological effect to the standard photon fractionation schedule of 2 Gy per fraction, NTD gives a clearer indication of the quality of the nonstandard treatment regime.

2.3.4. Equivalent Uniform Dose.

Equivalent uniform dose was first proposed by Niemerko[31, 32]. The fundamental idea of EUD is that it is the uniform dose distributed through a region of interest (ROI) that yields the same biological effect as the inhomogeneous dose distribution that was actually delivered to the ROI.

EUD can be defined in two ways. First, the mechanistic model, proposed by Niemierko in 1997[31], is referred to as the cell killing-based equivalent uniform dose (cEUD) by the American Association of Physicists in Medicine Task Group 166[33]. It was original only applied to targets.

The other model for EUD, referred to as generalized equivalent uniform dose (gEUD) by AAPM TG 166[33] and others, is an empirical model that generalized EUD to also apply to normal tissue as was proposed by Niemierko in 1999[32].

2.3.4.a. Cell Killing-Based Equivalent Uniform Dose (cEUD).

As previously stated, this model for EUD was originally derived to account for dose inhomogeneity within the PTV. In its simplest form cEUD is given by the equation[31, 33]:

$$cEUD = D_{ref} \cdot \frac{\ln\left[\sum_{i=1}^{N} v_i \cdot (SF_2)^{D_i/D_{ref}}\right]}{\ln(SF_2)}. \quad (22)$$

- D_{ref} is the reference dose (2 Gy).
- v_i is the partial volume receiving a dose of D_i.
- SF_2 is the surviving fraction for a reference dose of 2 Gy.

Neimeirko's paper[31] also derived equations for EUD that account for absolute volume effect (larger tumors need larger dose), nonuniform spatial distribution of clonogen in tumors, and a dose per fraction effect.

McGary et al.[34] showed the need for caution when using cEUD. They found that cEUD was more sensitive to high inhomogeneity and the choice of the radiological parameters ,α and β, than Neimeirko originally reported.

2.3.4.b. Generalized Equivalent Uniform Dose (gEUD).

Neimeirko presented the concept of gEUD at the 41st Annual Meeting of AAPM in 1999[32]. This form of EUD is an empirical model that is based on an analysis of outcomes rather than the use of the Linear-Quadratic model of cell survival. This form of EUD can also be applied to normal tissue. It is given by the equation:

$$gEUD = (\sum_{i=1}^{N} v_i D_i^a)^{1/a}. \quad (23)$$

- v_i and D_i are the same as in equation 22.
- a is a tissue-specific parameter.

The value of the tissue-specific parameter, a, depends on the type of tissue being analyzed. For large positive values of a, the gEUD approaches the maximum dose in the region of interest (ROI). These values would correspond to serial type normal tissue such as the spinal cord. The gEUD approaches the minimum dose for large negative a values thus these values of a are used for tumors. Setting a equal to 1 yields a gEUD that is equal to the mean dose which is useful for parallel type normal tissue.

As stated in a previous section, Henriquez et al.[35] showed that caution should be used when using gEUD for regions of high inhomogeneous dose distributions.

Chapter 3. The Impact of CT-Scan Energy on Range Calculation in Proton Therapy Planning

Kevin Grantham[1], Hua Li[2], Tianyu Zhao[2], Eric Klein[2] ([1]University of Missouri, Columbia, MO, [2]Washington University, St. Louis, MO)

NOTE: An edited version of this chapter was accepted for publication in The Journal of Applied Clinical Medical Physics (JACMP) in 6/2015.

3.1. Abstract.

Purpose: To investigate the impact of tube potential (kVp) on the CT number (HU) to proton stopping power ratio (PSPR) conversion. The range and dosimetric change introduced by a mismatch in kVp used for the CT scan, and the HU to PSPR table, based on a specific kVp, used to calculate dose are analyzed. **Methods:** Three HU to PSPR curves, corresponding to three kVp settings on the CT scanner, were created. A treatment plan was created for a single beam in a water phantom passing through a wredge-shaped bone heterogeneity. The dose was recalculated by changing only the HU to PSPR table used in the dose calculation. The change in the position of the distal 90% isodose line was recorded as a function of heterogeneity thickness along the beam path. The dosimetric impact of a mismatch in kVp between the CT and the HU to PSPR table was investigated by repeating this procedure for five clinical plans comparing DVH data and dose difference distributions. **Results:** The HU to PSPR tables diverge for CT numbers greater than 200 HU. In the phantom plan, the divergence of the tables resulted

in a difference in range of 1.6 mm per cm of bone in the beam path, for the HU used. For the clinical plans, the dosimetric effect of a kVp mismatch depends on the amount of bone in the beam path and the proximity of OAR's to the distal range of the planned beams. **Conclusion:** A mismatch in kVp between the CT and the HU to PSPR table can introduce inaccuracy in the proton beam range. For dense bone, the measured range difference was approximately 1.6 mm per cm of bone along the beam path. However, the clinical cases analyzed showed a range change of 1mm or less. Caution is merited when such a mismatch may occur.

Keywords: proton therapy, proton planning, CT number, proton stopping power ratio

3.2. Introduction.

A major source of range uncertainty in proton therapy is in the conversion of computed tomography (CT) number, or Houndsfield units (HU), to the corresponding relative proton stopping power ratios (PSPR) for dose calculation. It is therefore important to characterize the CT simulator used for proton therapy to investigate the possible effects of; scanning location, scanning energy, scanning protocol, and the presence of high Z material, on the measured relationship between the CT number of various materials and their corresponding PSPR.

Of particular interest is the effect of tube potential (kVp) on the conversion. It is well known that the CT number is dependent on the energy spectrum of the scanner.[36, 37] Cropp et al.[38] demonstrated kVp dependence in the CT number. Bai et al.[39] showed a kVp dependence in the determination of the linear attenuation coefficient in PET-CT and

SPECT-CT applications. The dependence of CT number on kVp is in fact the basis for dual energy CT applications.[36, 40] Based on the aforementioned studies, it should be clear that there would be a kVp dependence for the CT number to PSPR table as well.

Schneider et al.[11] cited the results presented by McCullough and Holmes[41], showing that the CT number does not significantly change with scan energy as justification for not including it in their development of the stochiometric method of calculating the CT number to PSPR conversion. Schaffner and Pedroni[12], following the methods of Schneider et al., did not include the CT scan kVp in their study. Based on these studies, it is common practice for proton therapy clinics to only utilize a single CT number to PSPR table in their treatment planning systems.

The McCullough and Holmes study was limited to scan energies of 120 and 140 kVp. For lower energy scans such as 80 or 90 kVp, photoelectric interactions would be expected to increase, particularly in high-Z material such as bone. Increased photoelectric interactions result in an increased measured CT number for high-z tissues at low kVp compared to the same tissues at higher energies. Additionally, Mustafa and Jackson[42] showed that the CT number was dependent on the scan kVp particularly for high Z/high density materials.

Scanning at a lower kVp might be desirable in order to decrease imaging dose to normal tissue for pediatric patients. Siegel et al.[43] reported a 3.5 cGy reduction in dose for an 80 kVp scan of an 8 cm cylindrical phantom compared to a 140 kVp scan of the same phantom. The decrease in imaging from scanning at a lower kVp is small compared to the therapeutic dose. However, the imaging dose is predominately delivered to normal tissue so the dose reduction may be beneficial.

Moyers et al.[44] also studied the effect of kVp on the CT number to PSPR conversion. However, that study was limited to water, polycarbonate, polymethylmethacrylate (PMMA), and clear polystyrene. These are relatively low-Z/low density materials (near soft tissue equivalent). For these low-Z materials, Moyers et al. found ±2% difference in the CT number between 80 and 140 kVp compared to 120 kVp.

The purpose of this study is to show the dosimetric effect of a mismatch between the kVp of the planning CT and the kVp of the PSPR conversion table used to calculate dose, demonstrating the need to include verifying the scan energy of the planning CT as part of the patient quality assurance (QA) process.

3.3. Methods and Materials.

3.3.1. CT Number to PSPR Table Creation.

The CT simulator used in this study was a Brilliance 16-slice large bore spiral CT scanner (Philips Healthcare Andover, Massachusetts). Routine quality assurance tests are regularly performed on the CT simulator to ensure their performance is consistent with the recommendations of AAPM Task Group Report 66 [45]. Quality assurance test relevant to this study are: image noise (checked daily) and CT number accuracy (water tested daily, 7 materials checked monthly, and13 materials checked annually).

The CT-electron density (ED) phantom (CIRS model 062M Norfolk, VA) was scanned using a pelvis scan protocol, as shown in Figure 3.1. The scan parameters for this protocol were: 90 and 120 kVp, 300 effective mAs, collimator set to 16 x 1.5 mm, 0.5second rotation time, 0.688 pitch, standard resolution and standard filter. The phantom was scanned with a water equivalent insert at the top of the phantom (position

1) which was subsequently replaced with a titanium insert for a second set of scans. These scans were repeated with the phantom in three locations within the field of view (FOV) of the CT scanner: in the center of the FOV, at 6 cm up and 6 cm right, and at 5 cm left and 4 cm down. Two additional scans were performed at 140 kVp with the phantom centered in the FOV of the CT with and without the titanium insert.

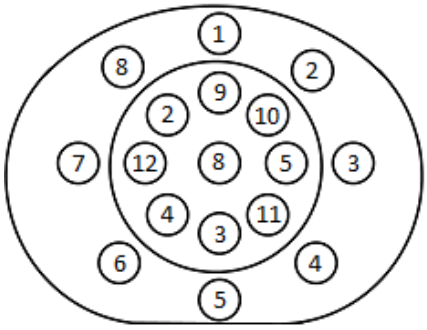

1. Water Equivalent or Titanium
2. Trabecular Bone
3. Liver
4. Breast(50/50)
5. Adipose
6. Water Syringe
7. 800 mg/cc Bone
8. Muscle
9. **Pelvis Protocol** - Lung (Exhale) **Brain Protocol** - Water Syringe or Titanium
10. 1250 mg/cc Bone
11. Lung (Inhale)
12. Lung (Exhale)

Figure. 3.1. A diagram of the electron density phantom showing the orientation and placement of the materials placed in the phantom for scans using the pelvis scanning protocol. For scans with high Z material the water equivalent insert at the top of the phantom was replaced with a titanium insert. For scans using the brain scanning protocol, only the center, circular section of the phantom was scanned with one of the Lung(Exhale) inserts replaced with either a water syringe or titanium for scans with high-Z material present.

The same procedure was followed using a brain protocol using only the center, circular section of the phantom shown in Figure 3.1. The scan parameters for this protocol were: 90 and 120 kVp, 500 effective mAs, collimator set to 16 x 1.5 mm, 0.5second rotation time, 0.563 pitch, standard resolution and standard filter. Like the

Pelvis protocol scans, the phantom was scanned at three locations within the FOV of the CT. At each location in the FOV two scans were performed, with titanium and with a liquid water syringe placed at position 9 in Figure 3.1. The phantom was only scanned in the center of the FOV for a tube potential of 140 kVp.

The CT scans that were acquired were then imported into our commercial treatment planning system (TPS), Eclipse v11 (Varian Oncology Systems Palo Alto, CA). CT numbers of the tissue substitute materials were measured using the area profile tool in Eclipse by recording the mean CT number within the area of interest for each material in the electron density phantom. The measured CT numbers were then sorted by the tube potential at which they were acquired and a mean CT number was calculated for each material averaged over all the phantom setups scanned. Three CT number to PSPR tables were produced from the mean CT number data using the stochiometric method described by Schneider et al.[11]

3.3.2. Uncertainty in the CT Number PSPR Conversion Tables.

The number of measurements contributing to the average CT number of the tissue substitute material used in the stochiometric calculation varied between 4 and 18 depending on kVp and tissue substitute. For instance, the CT number both inhale and exhale lung equivalent material was measured 4 times for the 140 kVp table. Whereas, the CT numbers of all soft tissue equivalent materials were measured 18 times for the 120 kVp tables.

For each kVp and tissue equivalent material the mean and standard deviation (SD) of the measured CT number was calculated. The uncertainty in the calculated CT number

to PSPR tables was calculated by performing the stochiometric calculation using the mean CT number ± SD. The limitations of the stochiometric method of calculating the CT number to PSPR table and uncertainty in the ICRU 44 [46] human tissues were not included in this study.

For the 140 kVp table, the CIRS phantom was only scanned at the center of the field of view of the CT simulator. Uncertainty due to phantom position was not explored for this kVp.

The 120 kVp CT number to PSPR conversion table was validated by IROC (Imaging and Radiation Oncology Core, Houston, TX). The tissue substitute materials in the CIRS phantom were used to evaluate the accuracy of the CT number to PSPR conversion tables with other kVp settings. For each material scanned, the CT number was used to calculate the expected PSPR from the conversion table with the corresponding kVp. The expected PSPR, calculated for a give material, should remain constant provided the kVp used to scan the material matched the kVp of the conversion table.

3.3.3. Phantom Verification of Range Change.

Three identical copies of a virtual rectangular water phantom (CT number set to 0 HU) with a wedge-shaped bone heterogeneity (CT number defined to be 1488 HU, the default value for bone in the TPS) placed in the beam path were created in our TPS. Each copy of the phantom was assigned a different CT number to PSPR table to calculate dose. The PSPR tables assigned to the phantoms corresponded to energies available: 90, 120, and 140 kVp. To measure the effect of scan energy on the proton range calculation, a

standard plan was created for each PSPR table and subsequently recalculated with a different PSPR tables via the creation of verification plans.

The difference in range between different PSRP tables was measured by the change in the position of the distal 90% isodose value between standard and verification plans relative to a rectangular structure placed distal to the target. A relationship between bone thickness in the beam path and the difference in proton range was obtained by measuring the change in range for several thicknesses of bone placed in the beam path.

3.3.4. Dosimetric Impact of PSPR Table kVp Mismatch in Patients.

To demonstrate the dosimetric impact of a mismatch in kVp between the planning CT and the HU to PSPR table, five clinical plans representing three anatomical sites were chosen. A description of the clinical cases used in this study is shown in Table 1 including the prescribed relative biological effective dose in cobalt-cGy-equivalent (CcGE). For this study, each clinical plan was treated as if it had been inappropriately scanned using 90 kVp, but planned assuming they were scanned at 120 kVp. Therefore, the 120 kVp PSPR table was used to calculate dose. The mismatch between the scan kVp and the PSPR kVp would likely manifest as an underestimation of the range of the proton beams, particularly when bone is present in the beam path, compromising the quality of the delivered plan.

Utilizing the same methods as used with the phantom discussed earlier the dosimetric impact of this hypothetical kVp mismatch can be assessed. Using verification plans to ensure that no change in the beam geometry occurred, the dose for all patient plans were recalculated using the 90 kVp PSPR table rather than the 120 kVp table.

Table 3.1. A description of the clinical plans used in this study.

Patient	Plan Description	Number of Fields	Perscription Dose (CcGE)
1	Brain Boost	2	1080
2	Brain	3	4500
3	Prostate Boost	2	3420
4	Right Lung	2	4000
5	Left Lung	3	6000

Two methods were used to evaluate the impact of changing the PSPR table. First, the dose-volume histogram (DVH) data from the clinical plan was compared to the DVH data for the recalculated plan. This method demonstrated a change in the dose distribution has occurred for nearby organs at risk (OAR). However, the method lacks the geometry information to fully visualize how the dose distribution changed by calculating the dose with a PSPR table based on a different kVp.

Visualization of the change in the dose distribution was achieved by exporting the RT-Dose files for the clinical and recalculated plans to MATLAB R2012a (Mathworks Natick, MA) where dose from the clinical plan was subtracted from the recalculated plan. This difference was then placed into a new RT-Dose file that was imported back into the TPS giving a three-dimensional visualization of magnitude and location of differences between the two plans.

3.4. Results.

3.4.1. Energy Dependence.

Figure 3.2 shows the calculated CT number to PSPR tables for all energies measured. The error bars in Figure 3.2 show the uncertainty in the CT number for each human tissue used in the stochiometric calculation of the tables. For comparison between the kVp settings, each table was divided into three sections, low density tissue, soft tissue, and high density tissue. A linear fit was applied to each section of tissue such that each table was described parametrically by three linear equations. Intercomparison of the tables was then performed by comparing the PSPRs calculated using the linear fit appropriate for the chosen CT numbers.

For tissues with a CT number less than 200 HU, there was less than 3% variation in the calculated PSPR between the different kVp settings. For tissues with a CT number greater than 200 HU, the slopes of the conversion tables decrease with decreasing kVp.

There was an 8% difference in the slope of the linear fits of the 120 kVp and 140 kVp tables for tissues having a CT number greater than 200 HU. This difference in the slope equates to less than 3.5% difference in the calculated PSPR up to a CT number of 2600 HU. For the 90 kVp table, the slope of the linear fit is 23% less than that of the 120 kVp table, resulting in greater than 3.5% difference in the calculated PSPR for tissues with CT numbers above 360 HU.

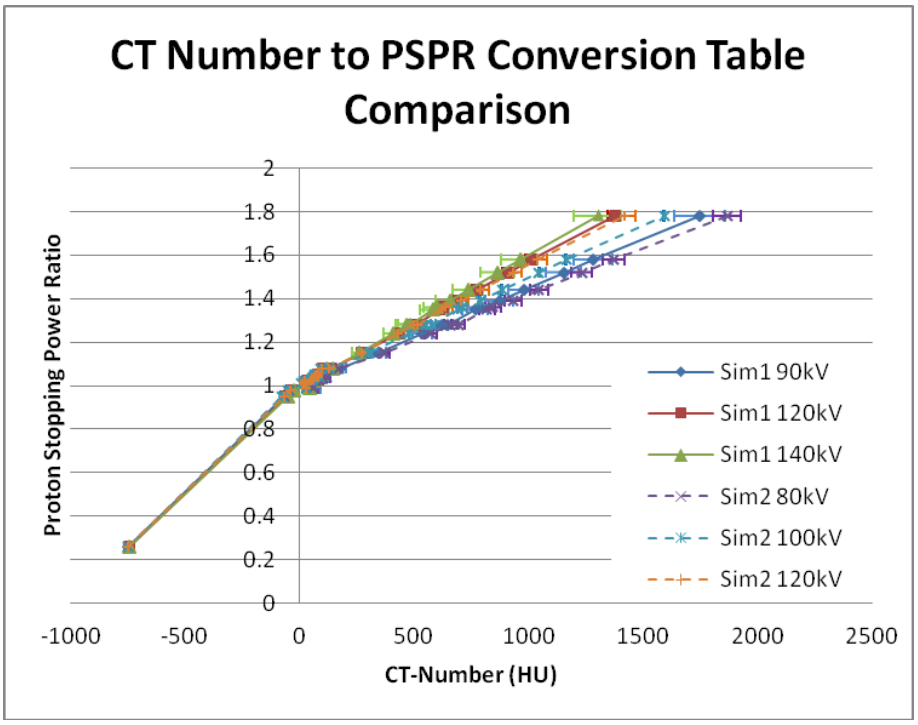

Figure. 3.2. A comparison of the HU to PSPR tables created for two CT simulators and the three available kVp's. The error bars represent the uncertainty in the calculated CT number for each of the given ICRU 44[46] tissues used in the stochiometric calculation of the tables.

3.4.2. Range Shift in Phantom.

The calculated range shift seen in the phantom between the 120 kVp and 140 kVp tables was minimal as would be expected given the similarity between the tables. However, when the field calculated using the 90 kVp table was recalculated using the 120 kVp table, the calculated range decreased. Figure 3.3 shows the change in the 90% isodose level and a plot of the change in the calculated proton beam range vs. the thickness of bone in the beam path. The change in range in the phantom was calculated to be 1.6 mm per cm of bone in the beam path.

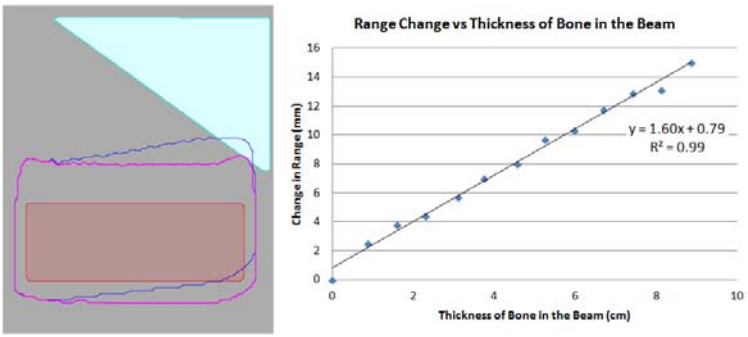

Figure. 3.3. Left: A comparison of the position of the 90% isodose level calculated for the same proton field with the dose calculated using the 90 kVp PSPR conversion table (pink) and the 120 kVp PSPR conversion table (blue). Right: A plot of the change in proton range between the 90 kVp and 120 kVp PSPR tables vs. thickness of bone (CT number= 1488) in the beam path. A linear fit to this data give a range change of 1.6 mm change in range per cm of bone in the beam path. (R^2=0.99 for the fit).

3.4.3. Patient Studies.

Figures 3.4 and 3.5 show the dose difference maps for the two brain treatments. In each figure, the contours for the CTV and relevant critical structures are shown. For Patient 1 (Figure 3.4), a mismatch in kVp would result in an increase in the dose to the brain and brainstem. Patient 2 (Figure 3.5) also shows an increase in dose to both optic nerves, the pituitary gland, the left temporal lobe of the brain, the left hippocampus, and the brainstem. Additionally, the dose to the right cochlea of Patient 2 would increase by approximately 500 CcGE.

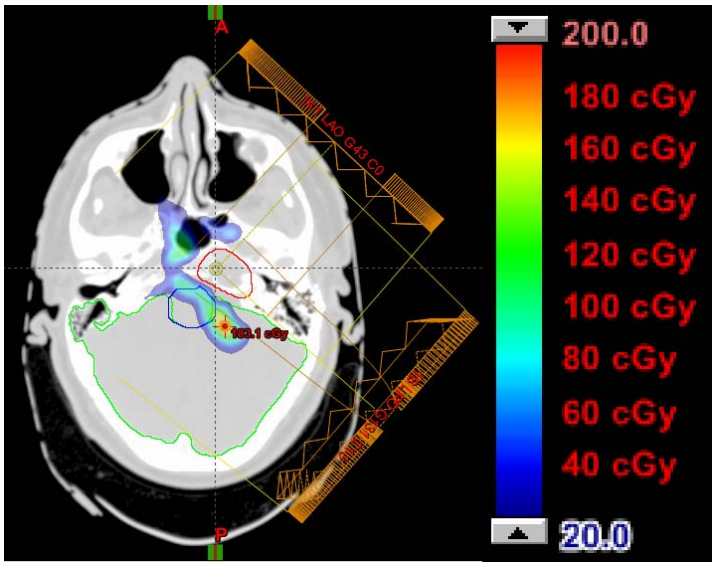

Figure. 3.4. Patient 1. Prescribed dose of 1080 CcGE. Calculated dose difference for a two-field boost in the brain. The contours for the CTV, brain, and brainstem are shown.

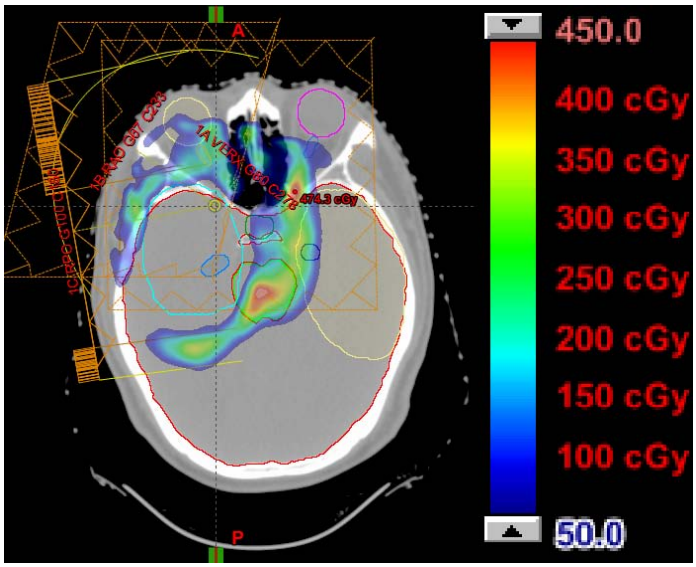

Figure. 3.5. Patient 2. Prescribed dose of 4500 CcGE. Calculated dose difference for a three-field plan in the brain. The contours of the CTV, brain, brainstem,left temporal lobe, hippocampus (left and right), pituitary gland, eyes(left and right), and optic nerve(left and right) are shown.

For the prostate treatment (Patient 3) using opposing lateral beams, there is significant bone in the beam path but the location of the critical organs is such that the range difference caused by changing the PSPR table is not sufficient to cause a significant change in the DVH data. However, as shown in the dose difference map (Figure 3.6), the dose calculated with the 90 kVp table is significantly higher in the normal tissue between the CTV and the femoral heads. This tissue is not associated with a specific OAR. Therefore, it would be unlikely that the dose difference would be detected using DVH analysis.

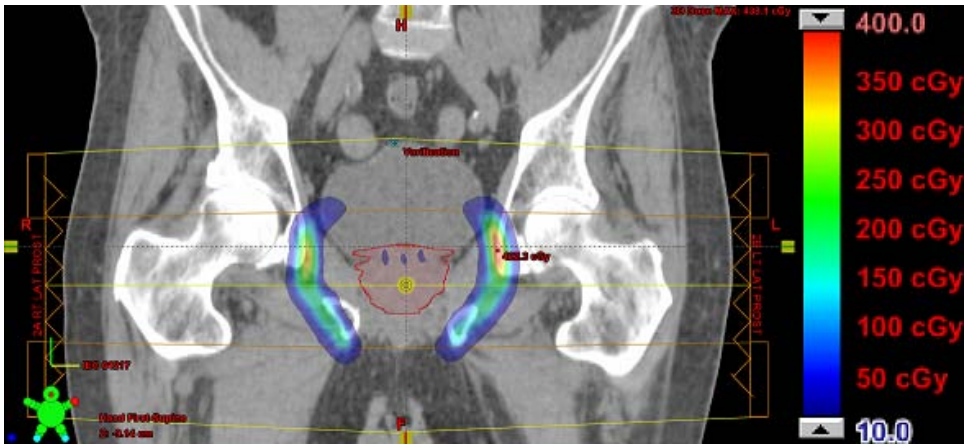

Figure. 3.6. Patient 3. Prescribed dose of 3420 CcGE. Calculated dose difference for a two-field boost treatment to the prostate. The contours of the CTV, bladder and femoral heads are shown.

For the two lung treatments (Patients 4 and 5), the situation is more complex. There were regions with bone present and no critical organ close enough distally to cause a discernible change in the DVH. There are also regions where there is no bone in the proton beam path, and thus no change in range occurs. Finally, there are regions where there is bone present that causes increased dose to a distally located critical organ.

However, the volume of the critical organ is sufficiently large compared to the volume of the dose increase that a change in the DVH is not apparent. Figures 3.7 and 3.8 show the dose difference maps between the two PSPR tables for the lung treatments. The regions showing the greatest dose difference correlate to regions near the distal edge of the target with the most bone present in the beam path.

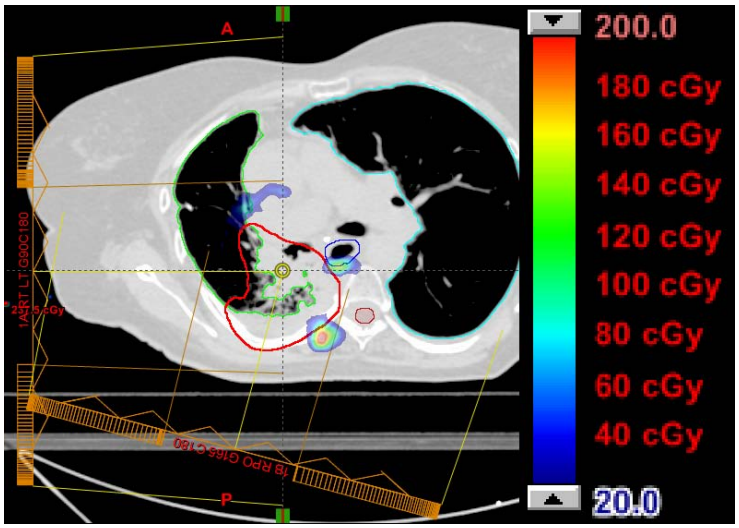

Figure. 3.7. Patient 4. Prescribed dose of 4000 CcGE. Calculated dose difference for a two-field treatment to the left lung. The contours of the CTV, Lung (left and right), spinal cord, and esophagus are shown.

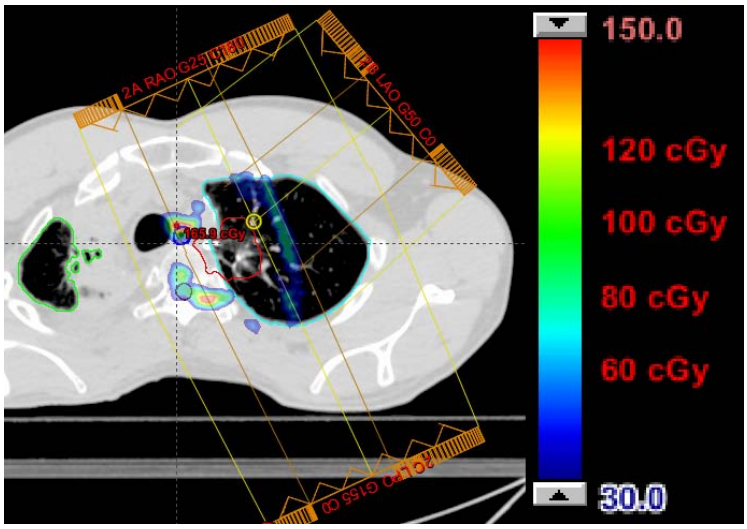

Figure. 3.8. Patient 5. Prescribed dose of 6000 CcGE. Calculated dose difference for a three-field treatment to the right lung. The contours of the CTV, Lung (left and right), spinal cord, and esophagus are shown.

3.5. Discussion.

A major source of range uncertainty in proton therapy is in the conversion of CT number to the corresponding relative proton stopping power ratios (PSPR) for dose calculation. Schneider et al.[11] and Shaffner and Pedroni[12] showed that using a stochiometric method for calculating the PSPR from the CT number is adequate for obtaining this conversion. However, while beam hardening is included as a source of uncertainty in the CT number, the impact of CT scan kVp on the CT number is not adequately included in their method. Schneider et al.[11] referenced a study by McCullough and Holmes[41] stating that the CT number does not change significantly with scan energy. We found that while this is true for soft tissue, for bone the higher Z introduces a higher photoelectric component of attenuation which would potentially lead to a substantially higher CT number in dense bone for lower energy scans.

In Figure 3.2, the error bars represent the uncertainty in the calculated CT number for the given PSPR of the ICRU 44 human tissues modeled. This uncertainty was calculated by performing the stochiometric calculation with the uncertainty in the measured CT number of the tissue equivalent materials included.

For the tube potentials used in this study, the uncertainty in the measured CT number of the tissue substitute materials was consistent with the total CT number uncertainties for lung, soft tissue, and bone reported by Yang. In that study, the imaging uncertainty varied from: 2.9% at 140 kVp to 3.6% at 80 kVp for lung tissue, 0.58% at 140 kVp to 0.61% at 80 kVp for soft tissue, and 2.1% to 2.5% for bone tissue [47].

The accuracy of the CT number to PSPR conversion tables was evaluated. For each of the tissue substitute materials used, the PSPR, calculated from the tables, was within 3% of the 120 kVp table for CT Sim 1. The conversion table from CT Sim 1 at 120 kVp was used as a baseline because it had a third-party evaluation (IROC).

Possible explanations for the difference in the DVH comparisons between the brain and the other cases include; either there is not a sufficient amount of bone present in the beam path to cause a significant change in the beam range, or the OAR's are sufficiently separated from the distal range of the proton beams that the change in the proton range does not change the OAR dose. A third, and more likely, explanation for the difference in the DVH comparisons is a combination of both explanations.

When planning for patients with intracranial targets, it is very difficult to place a beam that does not have an OAR near its distal range because everything within the skull is essentially a critical structure. It is also, not possible to deliver a beam to the brain that does not pass through bone. The combination of these factors results in the DVH data

being different for the same plan calculated using different PSPR tables.

In all of the clinical cases in this study a mismatch in the kVp of the planning CT and the CT number to PSPR table resulted in a range change (i.e. change in the position of the 90% isodose level) of 1 mm or less. This suggests that in many cases, a mismatch in kVp would be unlikely to cause an underdose of the target based on the margins prescribed in the plans. However, a mismatch could contribute to higher than expected dose to OAR's near the distal edge of a field.

3.6. Conclusion.

The degree to which the CT number varies with scan energy creates an increased level of uncertainty in the PSPR for high Z material such as bone unless the kVp of the planning CT is matched with the kVp of the CT number to PSPR conversion table. This increased uncertainty is minimal for lung and soft tissue.

In the clinical cases studied the measured change in range caused by a mismatch in kVp was ~1 mm. Based on these results, it is likely that current margin definitions (3.5% of the range) may be sufficient to prevent loss of target coverage in many cases. However, a 1 mm increase in the range of a proton field can cause a substantial increase in dose to structures located near the distal edge of the field.

Unlike treatment planning with photons and electrons, a mismatch between the kVp of the planning CT and the kVp of the CT number to PSPR conversion table can substantially impact the quality of the treatment. With new proton therapy centers opening, this study is an important reminder to use caution when a mismatch might occur and to understand what the impact would be for their CT simulator.

Chapter 4. Uncertainty Amplification in "Field of the Day" Proton Delivery Strategies

Kevin Grantham[1], Eric Klein[2] ([1]University of Missouri, Columbia, MO, [2]Washington University, St. Louis, MO)

4.1. Abstract.

Purpose: To evaluate of the impact of uncertainty on plan delivery, for proton therapy, a subset of the planned fields are delivered rather than delivering all planned fields for every fraction. **Materials and Methods:** Nominal proton treatment plans (NP) were created in a commercial treatment planning system to treat a spherical target to 54Gy using two or three fields. Uncertainty was simulated for four scenarios:, a unilateral introduction of 3cm of bone, or air, for 10 of 30 fractions, a 1cm shift for one of the fields for 10 of 30 fractions, and a 5° rotation of the patient for 10 of 30 fractions. In the three-field case, a 1cm bilateral shift was also tested. The full treatments were calculated using summed plans for multiple treatment delivery strategies. The treatment simulations were compared to each other, and to the nominal plans by calculating $D_{max,min,mean}$ along with $V_{90,95,98,99,100\%}$ for the target. For an organ at risk (OAR) placed contralateral to the introduced uncertainty, $D_{max,min,mean}$ were also compared. **Results:** The 5° rotation showed no significant difference from the NP. In all other cases, the introduced uncertainty degraded the treatment delivery. For the two-field treatments, the single-field per fraction delivery (SF) consistently showed a decrease in D_{min} compared to the other

treatment delivery strategies. The introduction of air and bone in the SF treatments decreased D_{min} by 1.5% and 20% respectively. With bone introduced, V_{95} and V_{90} decreased an additional 3% and 4%, for SF treatments. With air introduced, $D_{max,min,mean}$ for the OAR increased by 14, 16, and 20% respectively, for SF treatments. The three-field treatment simulations showed similar results. **Conclusions:** The effect of uncertainties can be amplified in daily delivery regimes using fewer than all planned fields. This should be balanced with the desire for increased patient throughput.

Keywords: proton therapy, uncertainty, systematic error

4.2. Introduction.

Many studies have evaluated the dosimetric impact of interfractional variation in proton therapy. Moyers et al.[10] , Thomas[48], and Park et al.[14] analyzed uncertainties for the purpose of defining the appropriate margins around the target to account for uncertainties. Vargas et al.[18], Sejpal et al.[16], and Liebl et al.[49] analyzed uncertainties to verify the appropriateness of their margins and determine at what level of setup error the prescribed margins fail. Engelsman et al.[21] analyzed uncertainty to evaluate the utility of various immobilization devices. In all of these studies, it is not clear that the daily delivery regime was included in their evaluations.

In passively scattered proton radiation therapy treatment planning, each individual field in the treatment plan is designed to be able to deliver the full prescription dose uniformly to the target. The fact that each individual field can deliver uniform dose to the target allows the option to only deliver a subset of the fields in the treatment plan on a

given treatment day. By rotating which fields are delivered during each treatment session, the accumulated dose delivered to the patient over the entire treatment will match the dose shown by the treatment plan. This is a common practice in proton therapy.[2]

An advantage of this delivery regime is that is reduces the time required to treat a patient. By reducing the treatment time, a greater number of patients can receive treatment in a day. A reduced treatment time can also be beneficial in terms of patient comfort in patient support devices thus reducing the possibility of intrafractional motion.

The primary assumption in using this technique is that the total dose delivered to the patient is the same regardless of the delivery regime. This assumption excludes the presence of uncertainties in the treatment delivery. Trofimov et al.[3] showed that the standard deviation in the position of the 98% isodose level was increased, on average, by 25% when the prostate is treated with alternating daily fields, rather than both lateral fields being delivered daily. Wang et al.[1] also showed that when there is a large unilateral anatomical change in prostate patients, delivering both lateral fields provides a benefit because one field can partially compensate for the dosimetric loss introduced by the other field.

Van Herk et al.[19] showed that the overall uncertainty in a treatment plan was related to the number of fractions in which the plan is delivered. This study presents simple, albeit exaggerated situations in which it is demonstrated that a similar relationship may exist with the number of daily fields delivered and uncertainty, for various delivery regimes.

4.3. Methods and Materials.

4.3.1. Two-Field Plan.

A nominal treatment plan using two fields was created in our treatment planning system (TPS), Eclipse v11 (Varian Oncology Systems, Palo Alto, CA) which uses the pencil-beam dose calculation algorithm described by Schaffner.[50] The nominal plan was designed to deliver 5400 cGy to a spherical target centrally located in a rectangular water phantom. Figure 4.1A and 4.1B show the beam arrangement and dose distribution for the two-field nominal plan respectively.

There are two primary sources of uncertainty evaluated by this study. The first category is the uncertainties stemming from a change in the patient anatomy such as bone or air pocket unexpectedly moving into a beam path, planned for soft tissue, resulting in a retraction or extension of the proton beam range beyond the introduced heterogeneity. The second category of uncertainties stem from misalignment of the patient resulting in translated or rotated dose distributions.

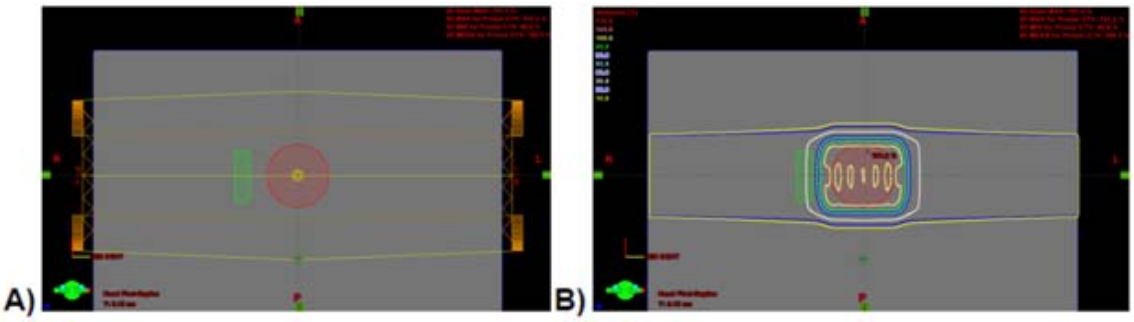

Figure 4.1. A) Beam arrangement for the two-beam nominal proton plan with target contoured in red and an organ at risk (OAR) contoured in green. B) Two-beam nominal dose distribution.

Figure 4.2 shows four of the five cases of uncertainty introduce into the nominal plans. The uncertainties simulated included four scenarios: a unilateral introduction of

3cm of air or bone for 10 of 30 fractions (Figure 4.2A and 4.2B respectively), a 1cm shift for one field for 10 of 30 fractions (Figure 4.2C), and a 5° rotation of the patient for 10 of 30 fractions (Figure 4.2D). The range, modulation, and compensator shape of the "uncertain" fields were strategically identical to the nominal plan.

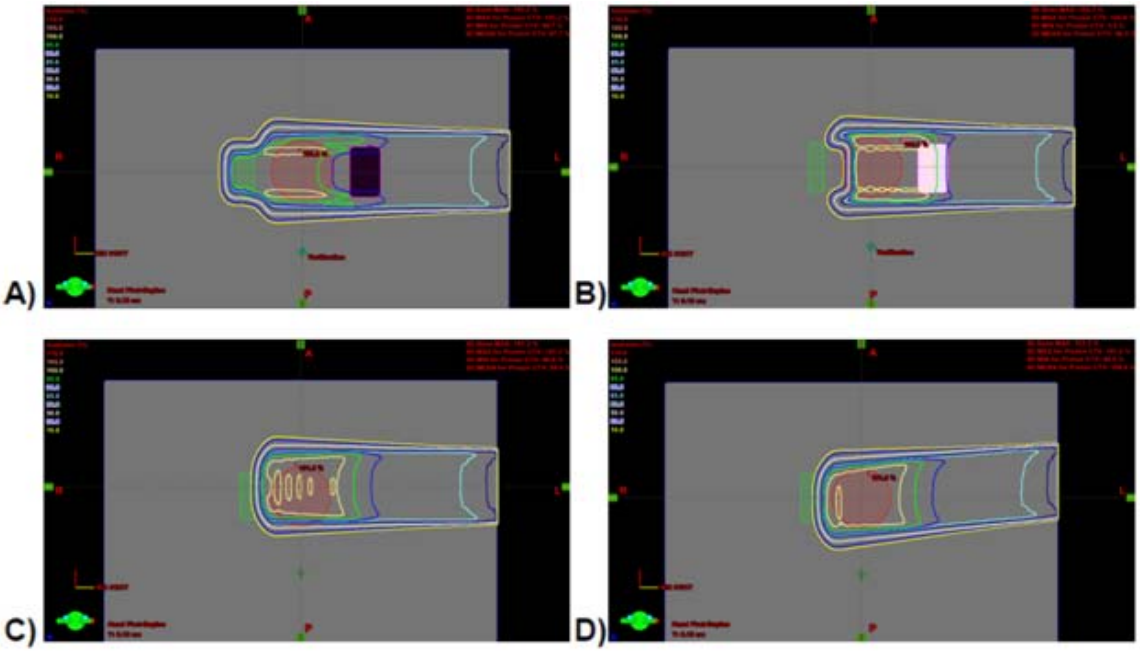

Figure 4.2. Four of five cases of uncertainty introduced into the nominal plan A) 3cm air, B) 3cm bone, C) 1 cm anterior shift, D) 5 degree rotation. The fifth case is only applied to the three-beam plan and is the same shift as C) but applied to both lateral beams.

The composite treatment plan was calculated by summing individual fields from the nominal plan and the fields with uncertainty included. The number of fractions and dose per fraction were adjusted to simulate single-field per fraction (*SF)*, subset of fields per fraction (*SSF)* and all fields treated per fraction (*ALL)* treatment regimes. The two-field results of the *SF* and *ALL* plan sums were compared to each other and the two-field nominal plan by calculating along with $V_{90,95,98,99,100\%}$. Values for D_{max}, $D_{,min}$, and D_{mean} were also compared for an OAR placed contralateral to the introduced uncertainty.

4.3.2. Three-Field Plan.

A nominal treatment plan using three fields was created in our TPS to deliver 5400 cGy to a spherical target centrally located in a rectangular water phantom. The phantom geometry used in the three-field treatment simulation was the same as was used in the two-field scenario. Figure 4.3A and 4.3B show the beam arrangement and dose distribution for the three-field nominal plan respectively.

In addition to the four cases of uncertainty shown in Figure 4.2, a 1cm bilateral shift for 10 of 30 fractions was also included for the three-field treatment simulation. As was the case in the two-field simulation, only the phantom geometry or the lateral position was changed. The range, modulation, and compensator shape of the "uncertain" fields were strategically identical to nominal plan.

The same quantities were calculated for the three-field simulation (Figure 4.3, A and B) as were calculated for the two-field simulations. Namely, $V_{90,95,98,99,100\%}$, D_{max}, $D_{,min}$, and D_{mean} for the target and D_{max}, $D_{,min}$, and D_{mean} for the OAR were calculated for the simulated treatment with uncertainty present. These values were then compared to the values calculated for the three-field nominal plan.

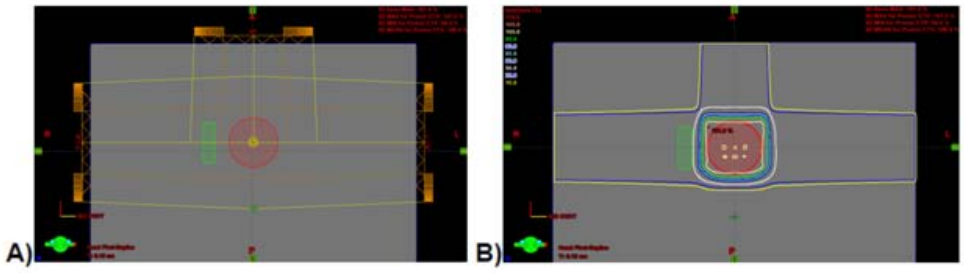

Figure 4.3. A) Beam arrangement for the three-beam nominal proton plan with target contoured in red and OAR contoured in green. B) Three-beam nominal dose distribution.

4.3.3. Treatment Delivery Time.

In order to assess the increase on room time for treating two fields verses one field, and three fields verses two fields, a study was conducted by reviewing treatment times from our Record and Verify system, MOSAIQ v2.5 (Elekta Inc., Atlanta, GA). The two-field cohort of patients consisted of prostate cancer (opposed lateral fields) and lung cancer patients. Time was assessed by subtracting out the additional time it took to treat, in this case a second field. A three-field cohort of patients composed of brain patients, lung patients, and liver patients was similarly analyzed.

4.4. Results.

4.4.1. Two-Field Plan.

Table 1 shows the relevant dose indices for the two-field simulated treatments. Except for the simulated treatment involving a 5 degree rotational shift, all of the simulated treatments showed some degree of plan degradation when compared to their respective nominal plan. In the rotated beam case, the quality of the simulated treatment was slightly improved compared to the nominal plan. Additionally, the *SF* (single-field per fraction) simulated treatment showed a slight improvement over the *ALL* (all fields delivered for every fraction) simulated treatment. However, this improvement would likely not be clinically relevant.

Table 4.1. Two-beam Plan Relevant Dosimetric Indices. The listed uncertainty was present in 10 of 30 fractions.

Plan Information		Target Dose							Organ at Risk Dose		
Uncertainty Added.	Delivery Regime	Min. Dose (cGy)	Mean Dose (cGy)	$V_{90\%}$	$V_{95\%}$	$V_{98\%}$	$V_{99\%}$	$V_{100\%}$	Max. Dose (cGy)	Min. Dose (cGy)	Mean Dose (cGy)
Nominal Plan.		5345	5425	100	100	100	100	92	3426	1812	2667
3 cm Bone.	All fields.	4553	5385	97	93	90	88	82	3162	1812	2635
	Single-field.	3701	5345	93	90	90	86	81	2903	1812	2604
3 cm Air.	All Beams.	5312	5401	100	100	100	94	48	4038	2238	3435
	Single-field.	5219	5376	100	100	94	80	25	4650	2627	4204
1 cm Shift.	All Beams.	5078	5416	100	99	97	95	85	3422	1812	2664
	Single-field.	4803	5405	100	98	95	92	83	3423	1812	2660
5 deg Rotation.	All Beams.	5346	5426	100	100	100	100	93	3372	1812	2658
	Single-field.	5346	5427	100	100	100	100	94	3318	1812	2648

The comparison of the two treatment regimes with 3 cm of air as the included uncertainty showed the least degradation in dose to the target compared to the nominal plan. However because of its location, the dose to the OAR showed the greatest increase when the void was introduced. In this case the *SF* treatment regime, the D_{max}, D_{min}, and D_{mean} were greater than the *ALL* treatment regime by 14%, 16%, and 20% respectively.

For the target, the greatest degradation from the nominal plan occurred when 3 cm of bone was included in the simulated treatment. Comparing the two treatment regimes the *SF* treatment show a decrease in all measured target indices with D_{min} being 20% higher in the *ALL* regime. The OAR doses were reduced when this uncertainty was included due to the bone heterogeneity reducing the range of the left lateral field.

The laterally shifted beam showed no significant change in dose to the OAR and a moderate change in the target indices compared to the nominal plan. Again, the *SF* treatment regime showed greater degradation than the *ALL* regime.

4.4.2. Three-Field Plan.

Tables 2 and 3 show the relevant dose indices for the three-field plan. The same indices were used for this plan as in the two-field plan. Table 2 shows the dose indices when heterogeneity is introduced into the beam path. Since the inclusion of a rotational shift did not show a significant change in the two-field plan, it was not tested for the three-field plan. Instead, a 1 cm shift in both lateral beams was tested. The relevant dose indices for unilateral and bilateral shifts are shown in Table 3.

Two modes of SSF (subset per fraction) treatment regimes were tested. First, a rotating set of two fields where no field was delivered for three consecutive fractions. In this mode, all three fields were weighted equally. The simulated daily fractions rotated between: the left lateral and AP fields, the right lateral and AP fields, and the right and left lateral fields.

Table 4.2. Three-beam Plan Relevant Dosimetric Indices. The listed uncertainty (3 cm of bone or 3 cm of air) introduced for 10 of 30 fractions.

Plan Information		Target Dose							Organ at Risk Dose		
Uncertainty Added.	Delivery Regime	Min. Dose (cGy)	Mean Dose (cGy)	$V_{90\%}$	$V_{95\%}$	$V_{98\%}$	$V_{99\%}$	$V_{100\%}$	Max. Dose (cGy)	Min. Dose (cGy)	Mean Dose (cGy)
Nominal Plan.		5370	5435	100	100	100	100	99	2338	1192	1779
3cm Bone.	All Fields.	4842	5408	100	95	92	90	87	2168	1198	1760
	Single-field.	3706	5355	93	90	88	86	83	1870	1193	1718
	Two-Field.	4558	5395	97	93	90	88	85	2084	1197	1750
	Two-Field. AP every fraction	4560	5400	97	94	90	89	86	1567	895	1306
3cm Air.	All Fields.	5344	5418	100	100	100	100	79	2753	1482	2293
	Single-field.	5220	5385	100	100	96	84	36	3588	1992	3317
	Two-Field.	5313	5410	100	100	100	99	65	2960	1618	2549
	Two-Field. AP every fraction	5314	5414	100	100	100	100	70	2433	1305	2106

Table 4.3. Three-beam Plan Relevant Dosimetric Indices. The listed uncertainty (1 cm unilateral or bilateral shift) introduced for 10 of 30 fractions.

Plan Information		Target Dose							Organ at Risk Dose		
Uncertainty Added.	Delivery Regime	Min. Dose (cGy)	Mean Dose (cGy)	$V_{90\%}$	$V_{95\%}$	$V_{98\%}$	$V_{99\%}$	$V_{100\%}$	Max. Dose (cGy)	Min. Dose (cGy)	Mean Dose (cGy)
Nominal Plan.		5370	5435	100	100	100	100	99	2338	1192	1779
1cm Unilateral Shift	All Fields.	5192	5428	100	100	99	98	92	2330	1193	1779
	Single-fields.	4826	5415	100	98	95	93	87	2325	1193	1774
	Two-Field.	5112	5430	100	100	98	96	92	2385	1194	1791
	Two-Field. AP every fraction.	5118	5432	100	100	98	96	91	1810	895	1341
1cm Bilateral Shift.	All Fields.	5024	5428	100	100	97	95	91	2406	868	1780
	Single-fields.	4275	5395	98	95	91	89	84	2325	206	1724
	Two-Field.	4837	5420	100	98	95	92	88	2384	705	1767
	Two-Field. AP every fraction.	4843	5422	100	98	95	92	88	1811	406	1317

The other SSF delivery mode delivered the AP field every fraction while alternating between the two lateral fields for each successive fraction. In this regime, the AP field delivers half of the prescribed dose to the target. The other half of the dose was split evenly between the two lateral fields.

With an uncertainty included, all simulated treatments showed some degree of degradation with respect to target coverage with respect to the nominal plan. The greatest degradation occurred when the bone heterogeneity was included. The degradation was particularly evident in the single-field per fraction (SF) treatment. The minimum dose to the target was decreased by 35% compared to the nominal plan. The other delivery regimes showed a 10% decrease when all fields were delivered and a 15% decrease for both SSF treatments.

With the void present, the least degradation in the target dose occurred relative to the other uncertainties simulated. However the void created the greatest increase in OAR dose. The single-field per fraction delivery mode resulted in a 53% increase in the maximum dose to the OAR relative to the nominal plan. The other treatment modes showed an increased maximum dose to the OAR of 17% when all field were delivered, 27% for the two-field per fraction regime with all fields equally weighted was delivered, and a 4% increase for the two-field per fraction regime was delivered with the AP field delivered for every fraction.

In Table 3, with the bilateral shift included, the minimum dose to the OAR was substantially reduced compared to the nominal plan. The primary reason for the reduction was that the OAR was placed within beam path of the right lateral field, and at the right edge of the AP field. A 1cm shift of the lateral fields would cause a decrease in

the minimum dose to the OAR because part of the OAR was no longer encompassed in the right lateral beam path. For the single-field per fraction case, part of the OAR was unirradiated for a greater portion of the treatment than in the other treatment regimes.

The *ALL* treatment regimen (all fields delivered for every fraction) resulted in treatments that were closest to the nominal plan in all cases. Also in all cases, the SF treatment regime (single-field per fraction) resulted in the treatments that were the most degraded compared to the nominal plan. The two SSF treatments were fairly equivalent to each other with respect to the target indices. Compared to the nominal plan, the target dose indices in the SSF treatments were much improved over the SF plans, but less desirable than the ALL regimes. With respect to the OAR, the SSF treatment regime in which the AP field was delivered, every fraction showed a significant dose reduction compared to the rotating subset of two fields.

4.4.3. Treatment Delivery Time.

For all patients examined the set up time and imaging time at patient entry time was averaged to be 9 minutes per patient. It also should be noted the average time for a patient to be off the table and exit the room is also an additional 3 minutes, hence the baseline of 12 minutes. This would increase to 20 minutes for anesthesia cases. On average, the additional field ranged anywhere from 5 to 8 minutes, with a weighted average of 6 minutes per extra field. This would mean that a 30 minute slot could be reduced to 24 minutes by removing one treatment field, or a 24 minutes slot could be reduced to 18 minutes for a two-field treatment technique. From department discussions

it was acknowledged that the 6 minutes time saving considering the overhead of setup, imaging, patient entry, and patient exit, was not worth the uncertainties induced.

4.5. Discussion.

The included uncertainties did not affect the ALL treatment regime (delivering all fields for every fraction) as much as the SF (one field per fraction) and SSF (two-field per fraction) treatments. For the ALL regime, the dose contribution of the uncertain fields to the total treatment dose was less. In all of the simulated treatments, the uncertain field was present in 10 of the 30 fractions. For the two-field plans, the uncertain fields contributed to 1/3 of the total dose to the phantom for the SF treatment. In the ALL treatment the contribution of the uncertain fields was reduced to 1/6 of the total dose.

For the three-field plans, the uncertain fields contribute 1/3 of the total dose to the phantom for the SF treatment. This is compared to 1/9 of the total dose for the ALL treatment regime. In both SSF treatments the uncertain fields constitute 1/6 of the total dose. The difference between D_{min} and D_{mean} in the nominal plan and the plans with uncertainty included shows a linear relationship with the number of fields per day, except in the case of D_{mean} for the three-field plan with a unilateral shift.

Another factor of increased uncertainty for SF and SSF treatment regimes lies in the fact that when these methods are used, the contribution to the total planned dose from each individual field is delivered in fewer fractions than when the all planned fields are delivered daily. Because, fewer fractions of each field are delivered the uncertainty in each field should increase in the same manner as shown by Van Herk et al.[19] In other words, for the two-field plan, the uncertainty in the total dose from treating with

alternating lateral fields should have equivalent uncertainty if the patient was treated with two fields per day, but with half the number of fractions. For the three-field plan, the dose uncertainty for the SF and SSF plans would be equivalent to treating with three fields per fraction for 1/3 and 2/3 of the prescribed number of fractions respectively. The experimental design of this study did not to verify this relationship.

An argument for using SF and SSF treatment regimes is the decreased treatment time. The time required to setup and image the patient does not change with delivery regime. Each treatment will always include the overhead of 8-10 minutes for the initial setup and imaging. The actual delivery time is small compared to the time required for setup. Delivering multiple fields per fraction would only moderately increase the total treatment time required for each patient and could significantly decrease the uncertainty in the delivery for patients receiving proton therapy.

One aspect not examined here is the uncertainty of the RBE at end of range with the largest concern being if a single-field per day was inadvertently ranging out at a critical organ and the affect of RBE thought theoretically to be higher than 1.1[51]. This would be another rationale for not treating with a single-field per fraction.

4.6. Conclusion.

Due to the nature of this study, it is unlikely that the relationship between the number of fields delivered for each fraction and the overall uncertainty in the treatment found here will directly translate to clinical situations. However, this study demonstrated that the effect of a single uncertainty introduced into a treatment plan is amplified for treatment regimes in which a rotating subset of fields from the treatment plan are

delivered daily. In treatment regimes in which all fields from the treatment plan are delivered each day, the other fields partially compensate for the introduced uncertainty. Due diligence is advised when delivering only a subset of the planned fields for each fraction.

Chapter 5. Single Field per Day vs. Multiple Fields per Day and the Impact on BED in Proton Therapy Treatment

Kevin Grantham[1], H. Omar Wooten[2], Tianyu Zhao[2], Eric Klein[2] ([1]University of Missouri, Columbia, MO, [2]Washington University, St. Louis, MO)

5.1. Abstract.

Purpose: A common practice in proton therapy is to deliver a rotating subset of fields from the treatment plan for the daily fractions. This study compares the impact this practice has on the biological effective dose (BED) versus delivering all planned fields daily with and without incorporating uncertainties. **Methods:** The RT-Dose file, structure set, and α/β ratios for all plans in this study were processed using in-house MATLAB code to return a new RT-Dose file containing the BED (including a proton RBE of 1.1) which was imported into a commercial treatment planning system for analysis. The BED calculation code was validated using a phantom with geometry approximating a prostate patient. One and two fields per fraction were simulated and compared with literature data. For a clinical prostate treatment, the role of uncertainty and treatment regime was evaluated for the BED of organs at risk (OAR) near the target when a systematic setup uncertainty was included in the plan. Additionally, for a three-field brain treatment, the BED variation was analyzed for 1, 2, or 3 fields per fraction treatment regimes. **Results:** For targets and regions of field overlap in the treatment plan, BED is not affected by delivery regimen. For the prostate phantom, the BED in the

femoral heads showed an increase of 20% when a single field was used rather than two fields. In the clinical prostate case, the included uncertainty lead to a 5% higher BED in the rectum near the field edge for the one field per fraction treatment. In the brain treatment, the minimum BED to the left optic nerve and the pituitary gland increased by 13% and 10% respectively, for a one-field regime compared to three-fields per fraction. Comparing the two-field and three-field regimes, the optic nerve BED was not significantly affected and the minimum pituitary BED was 4% higher for two fields per day. **Conclusion:** The impact, which is similar to hypofractionation, in regions of non-overlap of fields, significantly increases the BED to the involved tissues by as much as 20%. Care should be taken to avoid inadvertently sacrificing plan effectiveness in the interest of reduced treatment time.

5.2. Introduction.

A common practice in proton radiotherapy, is to plan a treatment consisting of multiple beams with a rotating subset of fields from the treatment plan delivered for the daily fractions. In the absence of uncertainties, this practice results in the same physical dose to the patient regardless of the treatment regime. However, for normal tissues, particularly in the entrance region of the beam, the dose received per fraction is increased when a subset of fields is delivered daily, rather than all fields are delivered. This results in an increase in biological effective dose (BED). This study compares the impact of delivery regime options on the BED.

Trofimov et al.[3] compared the effect of setup variation between single field per fraction and two fields per fraction treatment strategies for prostate cancer. They found that, for the single field per fraction treatment strategy, the standard deviation in the

position of the CTV, relative to the treated volume, was significantly higher. The standard deviation increased on average by 25% compared with treating both beams daily.

The effect of the fractionation schedule on the quality of the treatment has been previously studied by Wang et al.[1] and Engelsman et al.[2] Wang et al.[1] evaluated the impact on interfraction variations for prostate proton therapy. The delivery scheme was only part of the study. For ten low and intermediate risk prostate patients, their results showed significant improvement over single daily beam delivery schemes for situations involving large prostate shifts perpendicular to the beam direction or femoral head rotation on the order of 15 degrees. However, these extreme situations were rare in their study so the overall advantage of delivering both lateral beams daily was <0.6% for prostate coverage in each fraction. Also, the minimum dose to 97% of the volume of the target (D_{97}) was improved by less than 0.7cGy for all but one patient.

Engelsman et al.[2] studied the biologic effect delivering alternating subsets of fields for four different treatment sites: prostate, base of skull, lung and pancreas. They compared delivering all beams in a treatment every day to their clinical delivery scheme and single beam per day in terms of RBE-corrected absorbed dose, normalized total dose, and gEUD. The base of skull patient group showed a significant reduction in NTD to the left frontal lobe for the delivery scheme including all beams over treating a single beam per day, or the clinical protocol of rotating through six or seven unique field combinations daily. The lung patient group did not show any significant change in the NTD to the Lung-GTV when treated with all three beams daily compared with one or two beams daily. The Pancreas patient group showed a marked decrease in the NTD to

the small bowel when delivering all beams. Finally, for the prostate patient group, delivering both lateral beams every day resulted in a 30% reduction in NTD to the femoral heads. Engelsman et al.[2] also calculated the gEUD to critical normal tissues for each group. The gEUD was significantly reduced for nearly all normal tissue structures when all beams are delivered daily.

An issue with the work of Engelsman et al.[2] is that gEUD and NTD may not be the appropriate quantities to accurately describe the biological effect of protons in normal tissue. As shown by McGary et al.[4] and Henriquez et al.[5], the relevance of EUD breaks down regions with high dose gradients. Normal tissues near the lateral and distal edges of the proton field are subject to high dose gradients. Therefore the gEUD of normal tissue in these regions may not give an accurate representation of the biological effect in these particular regions.

Another minor issue with Engelsman's study is the use of NTD. The NTD normalizes to a fractionation regime of 200 cGy/fraction[6-8]. Only normal tissue very near the target receives dosages that high in magnitude. All other normal tissue receives much lower dose. For this reason, we bypass the normalization step in this study and only report BED.

When comparing the single field per fraction and multiple fields per fraction treatment schemes, it is important to remember, the physical dose absorbed by the patient is the same over the entire course of treatment. However, in tissues where the fields do not overlap the number of fractions resulting in that dose is significantly smaller when fewer daily fields are delivered. This results in an effect similar to hypofractionation of the dose to normal tissue in the entrance region of the fields and can lead to an increased

biological effect. The degree to which the biological effect is increased depends on the type of tissue involved and the α/β ratio of that tissue.

There are two aspects of the single field per fraction vs. multiple fields per fraction question that must be analyzed. First, to what extent does hypofractionation in single field treatment regimes contribute to a difference in BED for multiple field treatment regimes? The effect of treatment regime on the calculated BED was analyzed using a prostate phantom with opposed lateral fields and in a clinical three-field brain treatment. The purpose of this analysis was to verify that our BED calculation code produces results similar to the results reported by Engelsmann et al.[2]

Once the BED calculation code is validated, how much does the inclusion of systematic setup uncertainties impact the BED for single field vs. multiple field treatment regimes? This analysis was then performed for two clinical cases. The first clinical case was a patient with a two field prostate boost treatment using lateral opposing fields. The other clinical case was treated with three fields for a target in the brain.

5.2. Methods and Materials.

5.3.1. BED Calculation.

The BED calculations were performed using a MATLAB script[9], originally written to calculate BED in photon planning, modified to include the proton RBE (1.1). Figure 5.1 shows a diagram of the data flow from the original plan through the calculation of the BED distribution. The script takes as its input, the DICOM RT-Dose and RT-Structure files exported from the treatment plan, and a text file listing the appropriate α/β ratios for the structures listed in the RT-Structure file. For each point in

the RT-Dose file, the script determines the structure in which the point resides, and looks up the α/β ratio of that structure. The system then calculates the BED at that point using equation 20 from Chapter 2 Section 2.3.2.

$$BED_H = n_H(1.1d_H)\left[1 + \frac{(1.1d_H)}{(\alpha/\beta)_L}\right]. \quad (1)$$

After calculating the BED for all points in the RT-Dose file the script writes a new DICOM file containing the BED distribution of the imported plan. This new BED RT-Dose file can then be imported back into the treatment planning system for viewing. A dose-volume histogram can then be created using the imported BED data to create a BED-volume histogram (BEDVH).

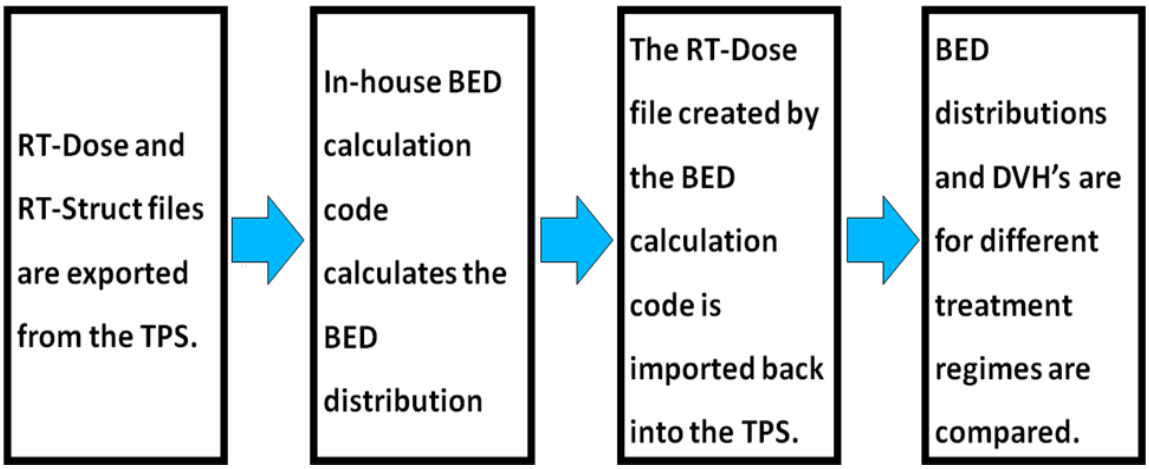

Figure 5.1. A diagram showing the flow of data from the original plan to the BED distributions.

5.3.2. BED Calculation Code Validation.

To verify the BED calculation code yields result similar to those of Engelsman et al.[2], two scenarios were chosen. The first scenario was a phantom with a geometry approximating the anatomy encountered for a prostate treatment with opposing lateral

fields. Treatment plans were produced in Eclipse Version 11 (Varian Oncology Systems Palo Alto, CA) to simulate delivery of one and two fields per fraction. The RT-Dose file, structure set, and α/β ratios were processed using the BED script to return a new RT-Dose file containing the BED (including a proton RBE of 1.1) which was then imported back into Eclipse for analysis.

A phantom prostate treatment utilizing opposing lateral beams (Figure 5.2) was planned to simulate delivery of: one, two, and three fields per fraction. A single field per fraction treatment was simulated by splitting the original treatment plan into a separate plan for each field. The prescription for each of these fields was the same dose per fraction as the original plan. The number of fractions was equal to the total number of fractions planned for the treatment divided by the number of fields in the original plan.

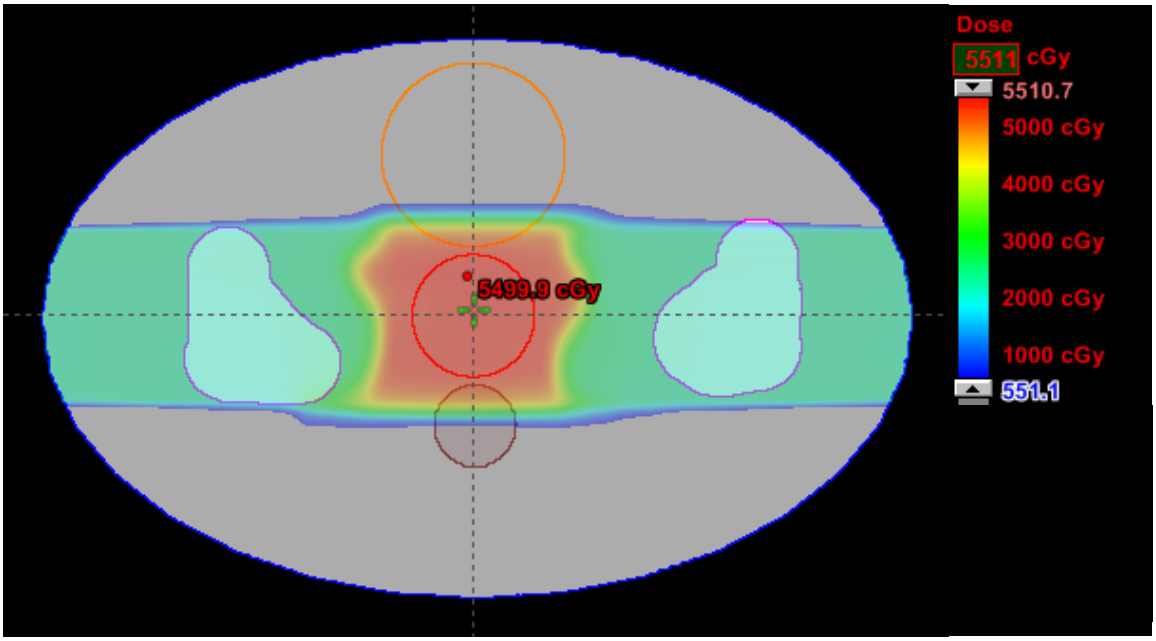

Figure 5.2. Planned physical dose distribution for a two-field phantom prostate treatment.

5.3.3. BED Including Uncertainties.

Utilizing the same methods of including uncertainties and the clinical cases described in chapter 4, the degree to which uncertainties impact the BED of a treatment for single field vs. multiple field treatment regimes can be determined.

For a clinical prostate boost plan, a treatment plan was created such that in half of the delivered fractions a 1 cm posterior shift was introduced in the left lateral field. The resulting physical dose for the treatment was independent of the treatment regime. Figure 5.3 shows the physical dose distribution for this plan. This plan was then processed with the BED calculation code for the two treatment regimes and the results were compared.

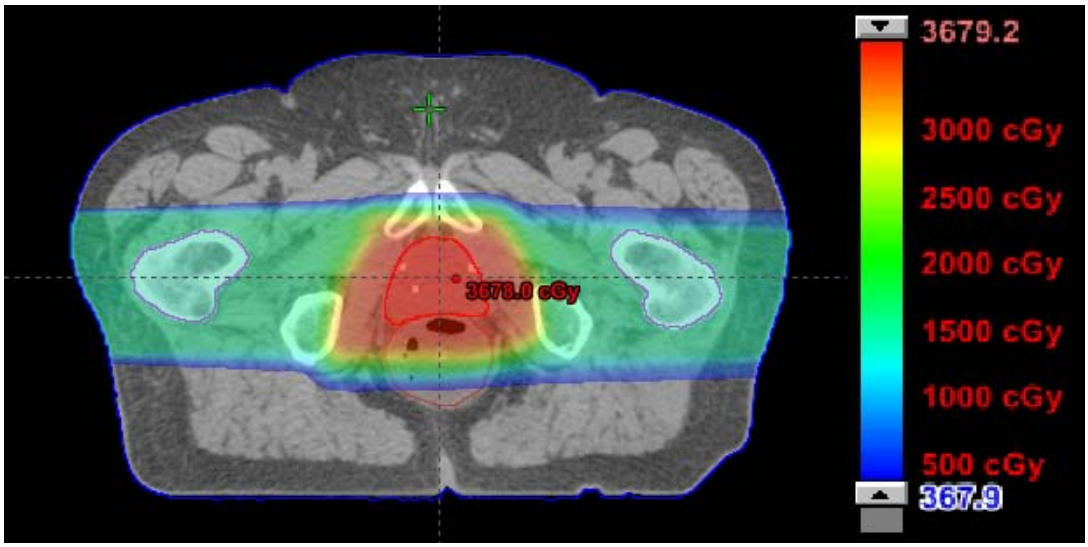

Figure 5.3. The physical dose distribution for a prostate boost plan with a 1 cm posterior shift introduced for the left lateral field in half of the delivered fractions

5.3.4. BED and Treatment Regime in a Three-Field Brain Treatment.

For a clinical case in which a target in the brain is planned with three fields, treatment with one, two, and three fields per fraction was simulated. The planned dose

for this patient's original plan is shown in Figure 5.4. As with the previous simulations, each treatment regime was simulated by creating separate treatment plans corresponding to possible field combinations that would be delivered in a given fraction. The original plan corresponds to the treatment with all three fields in every fraction. The one field per fraction was represented by a separate treatment plan for each planned field. A two field per fraction treatment was simulated using three two-field plans covering all distinct combinations of the three planned fields. In the one and two-field plans the prescription dose and the number of fractions was adjusted such that the total dose for the treatment was unchanged from the original prescription.

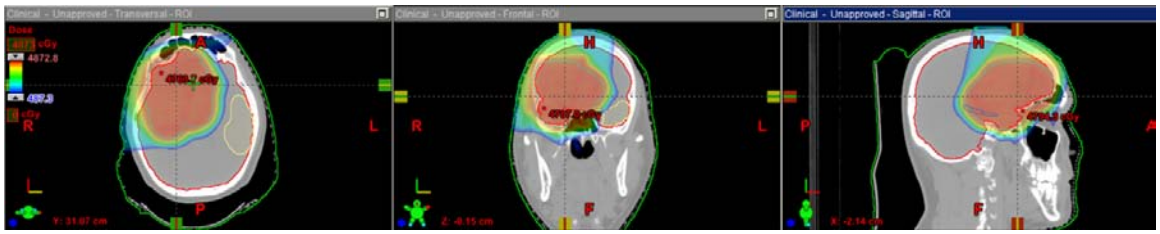

Figure 5.4. Planned physical dose for a three-field treatment in the brain.

Each of the seven treatment plans were then process with the BED calculation code. Summation of the single field plans yielded the calculated BED for a single-field per fraction treatment. Likewise, summation of the two-field plans yielded the BED for the two-field per fraction treatment. The calculated BED form each of the three treatment regimes were then compared to each other.

5.4. Results.

The BED calculated for the CTV in all plans used in this study was not affected by delivery regimen. The CTV receives approximately the same dose for each fraction in all treatment regimes. It is in normal tissue far from the CTV that the delivery regime impacts the calculated BED.

Figure 5.5 shows a comparison of the BED distribution for the prostate phantom. In the entrance region, BED in the single-field per fraction treatment was significantly higher than the two-fields per fraction treatment. Figure 5.6 shows a comparison of the biological effective DVH (BEDVH) between the two phantom treatment regimes. The BED to the femoral heads showed an increase of 20% when a single field was used rather than two fields.

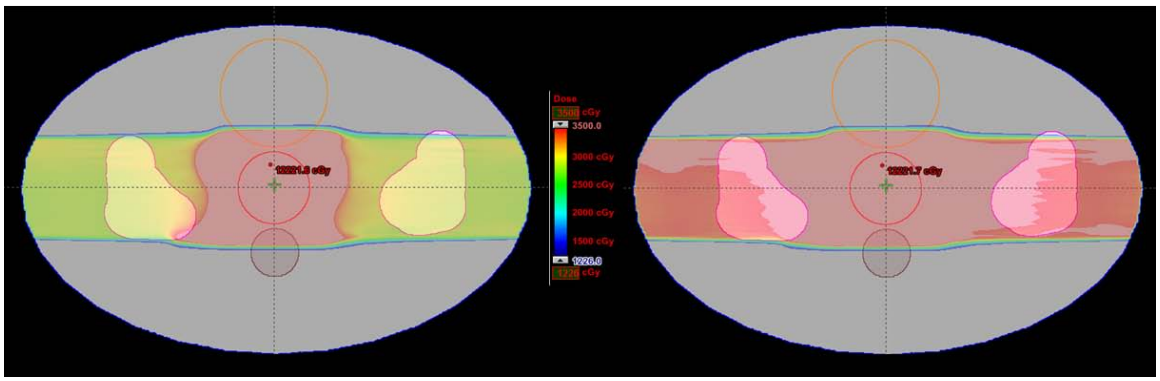

Figure 5.5. Side-by-side comparison of the BED distribution for the Prostate phantom plan. Right – two fields per fraction. Left – one field per fraction.

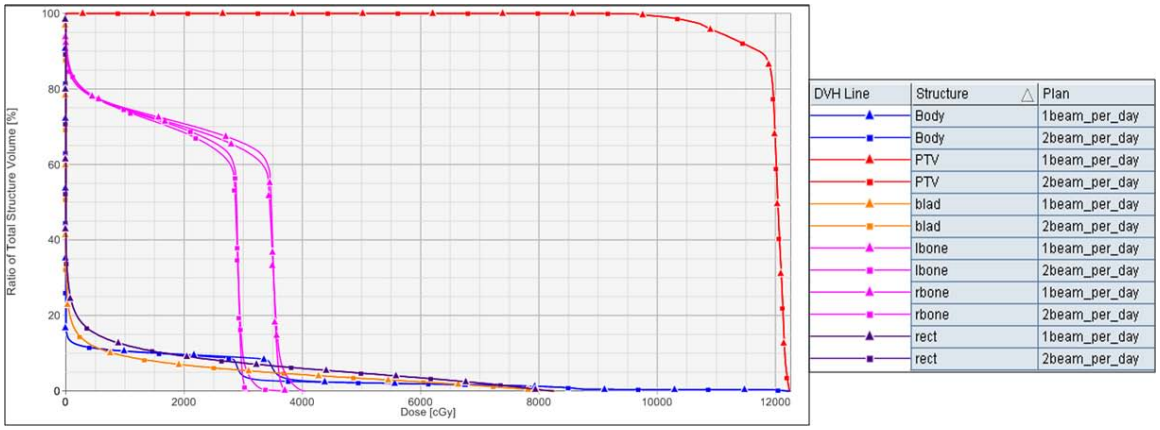

Figure 5.6. DVH comparing BED for a one-field per fraction treatment (triangles - ▲) and a two-field per fraction treatment (squares - ■). The BED for all structures are unchanged by the treatment regime except for the structures in the entrance regions of each beam where hypo-fractionation effects increase the BED to the structures. The α/β ratios used were: 1.5 for the PTV, 3 for all other structures.

Figure 5.7 shows a comparison of one, two, and three-field per fraction BED distributions for the clinical brain treatment. As with the phantom treatment**,** the entrance BED for a single-field per fraction treatment was significantly higher than the other treatment regimes.

5.4.1. BED Including Uncertainties.

While the physical dose for the prostate boost plan was unchanged with regard to the delivery regime. Like the previous treatments, the BED distribution was significantly different. Figure 5.8 shows the difference in the calculated BED distributions.

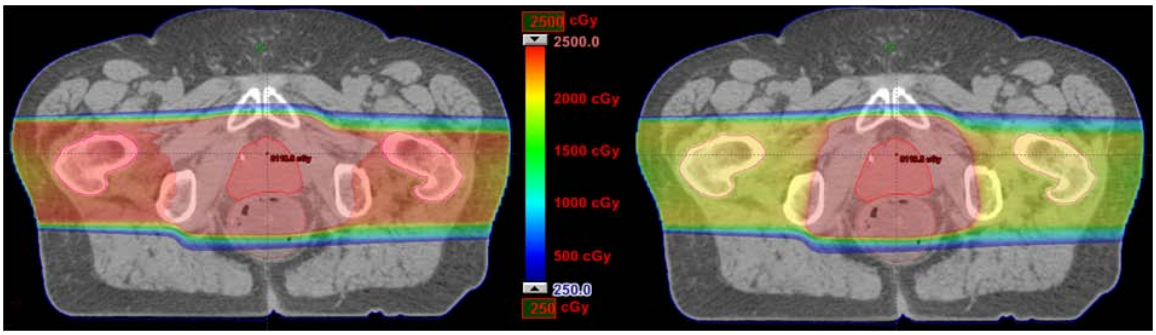

Figure 5.7. A comparison of the calculated BED distribution for a prostate boost treatment with a 1 cm posterior shift in the left lateral for half of the delivered fractions. Left: one field per fraction. Right: two fields per fraction.

The effect of the introduced uncertainty on the BED is not readily apparent in Figure 5.8. However, looking at the BED profile across the patient through the center of the rectum as shown in Figure 5.9, it is clear that uncertainty contributes to a higher BED to the rectum for the one field per fraction treatment.

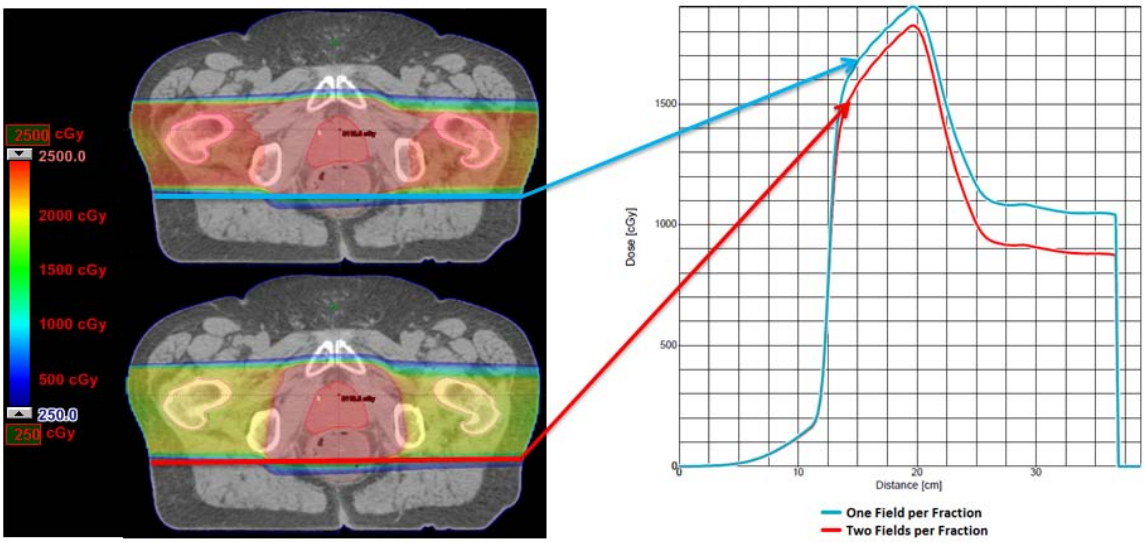

Figure 5.8. A comparison of the BED profiles across the patient through the region most affected by the introduced uncertainty.

In all cases, the BED in the CTV was unaffected by the treatment regime. The BED is a function of the dose per fraction. The CTV receives approximately the same dose in every fraction. Therefore, the BED for the CTV is independent of the treatment delivery regime.

5.4.2. BED and Treatment Regime in a Three-Field Brain Treatment.

Figure 5.10 shows the BED distributions for the one, two, and three- field treatment regimes. The BED distribution for the two-field per fraction treatment does not show a significant difference compared to the three-field treatment. The one-field treatment shows a greater BED in the region proximal to the CTV for the right posterior oblique field.

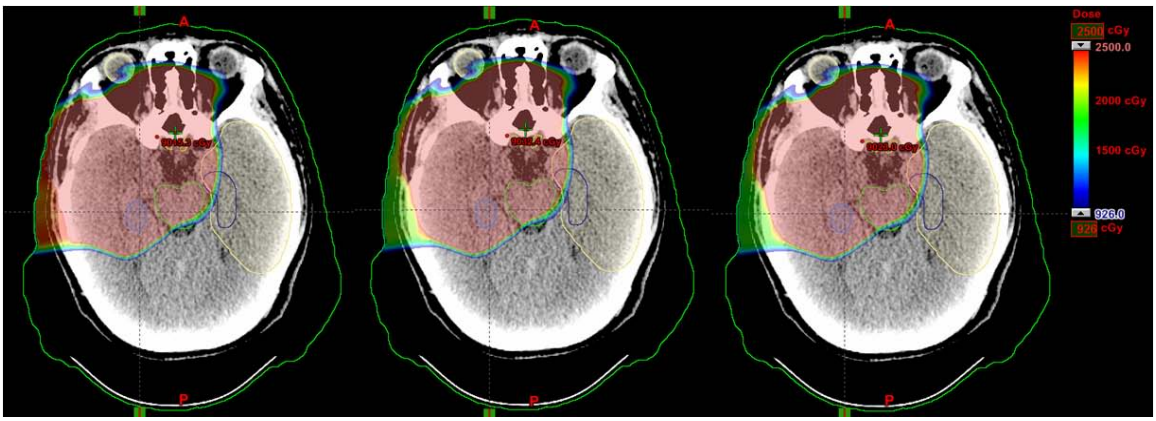

Figure 5.9. A comparison of one field per fraction (left), two fields per fraction center), and three fields per fraction (right). Note the difference between two fields per fraction and three fields per fraction is minimal compared to the difference between one field per fraction and two fields per fraction.

Figure 5.11 shows a comparison BEDVH for the brain treatment. The minimum BED to the left optic nerve and the pituitary gland increased by 13% and 10% respectively, for a one-field regime, compared to all-fields per fraction. Comparing the

two-field and three-field regimes, the optic nerve BED was not significantly affected while the minimum pituitary BED was 4% higher for two-fields per fraction.

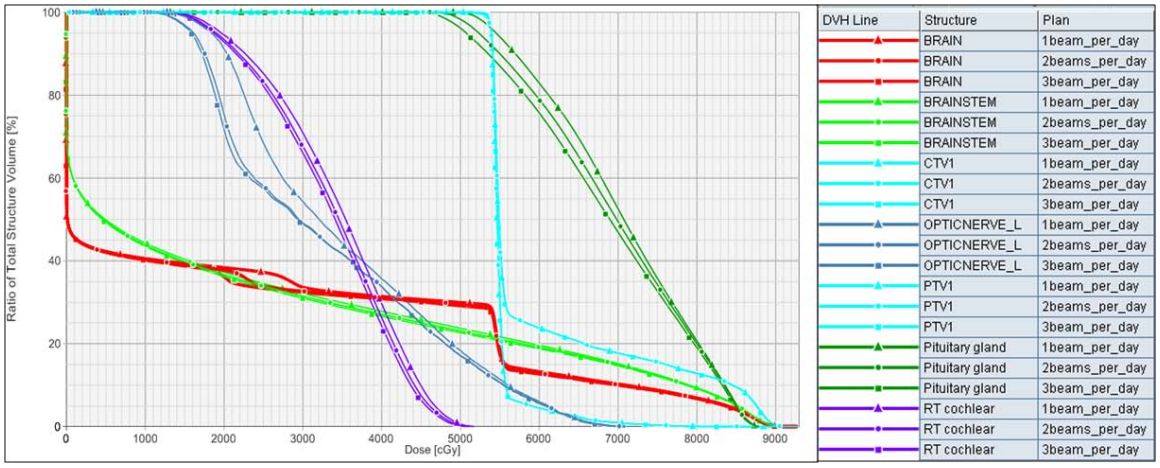

Figure 5.10. DVH comparing BED to relevant structures in one (triangles - ▲), two (circle - ●), and three (squares - ■) field per fraction treatment regimes. Note the change in BED for the left optic nerve (dark blue) and the pituitary gland (Dark Green). The α/β ratios used were: 10 for the CTV and PTV, 2 for all nerve tissue, and 3 for all other structures.

5.5. Discussion.

In the prostate phantom plan, the BED calculation code returned results, qualitatively, very similar to the prostate group reported by Engelsman et al.[2] A direct comparison between BED and NTD is not meaningful. However, since NTD and BED are linearly related, changes in each should be comparable. Differences between the femoral head dose in our phantom compared to Engelsman's prostate group stem from differing patient geometry, dose prescription, and different treatment delivery systems.

The shift included in the clinical prostate plan was quite large with a low probability occurrence clinically. However, it is not implausible particularly for newer single-room proton delivery systems where the gantry motion is limited. In such a system, the couch is heavily relied upon in order to deliver many fields. If the couch

calibration changed such that, at certain angles, the couch position was incorrect; a systematic uncertainty such as the one used in this study could manifest. A robust quality assurance procedure and vigilant therapists would limit the probability of such an event occurring.

In the three-field, brain treatment, fewer fields delivered per fraction resulted in higher calculated BED's for structures near the CTV particularly in the single-field per fraction treatment. For most structures the differences between the two-field and three-field treatments were very small. However, setup uncertainty was not included in this case. The rigid immobilization of patients being treated for targets within the brain minimizes uncertainty. However, the inclusion of setup uncertainties could dramatically affect the calculated BED in structures located near the CTV.

5.6. Conclusion.

The BED to the involved tissues outside the target can be increased by as much as 20% for single-field per fraction treatment regimes compared to treating all fields each fraction. Additionally, given an equivalent systematic error in the physical dose, the impact of the error is enhanced by treating with fewer fields per fraction. Care should be taken to avoid inadvertently sacrificing plan effectiveness in the interest of reduced treatment time.

Chapter 6. Modeling, Validation, and Application of a New Proton Therapy System Using a Monte-Carlo Environment Optimized for Protons

Kevin Grantham[1], Tianyu Zhao[2], Eric Klein[2] ([1]University of Missouri, Columbia, MO, [2]Washington University, St. Louis, MO)

6.1. Abstract.

Introduction: Monte-Carlo modeling is an important tool for understanding the behavior of therapeutic proton beams in heterogeneous media such as a patient. To gain confidence that a Monte-Carlo model is accurate in complex geometries and media, it must first be compared with measurement in simple situations. This study documents the validation of our Monte-Carlo Model and applies the model to a real patient for LET-dependent RBE calculation for comparing treatment delivery regimes. **Materials and Methods:** A model of the MEVION s250 Proton therapy system was created in the TOPAS Monte-Carlo environment using machine geometry and field shaping system information provided by the vendor. For 17 of 24 available treatment configurations, validation of the TOPAS model was performed by comparing the dose scored by TOPAS to the dose measurements obtained during the commissioning of the treatment planning system. A prostate patient's CT scan and treatment plan were imported into TOPAS. Dose and LET were scored for the patient plan and the LET-dependent RBE-corrected Dose was calculated. A comparison of delivery regime (one field/fraction vs two fields/fraction) was then performed. **Results:** Range measurements of the Monte-Carlo

simulations matched the measured data within 1mm. Distal fall-off of the simulated fields matched within <1mm. Lateral penumbra and field size measurements of the standard-sized square and half-beam blocked fields matched within 1mm at all three planes compared. A small difference was seen in the in-air profiles at doses <20%. The suspected cause of the difference was the aperture divergence. While the measured data utilized a divergent aperture, the Monte-Carlo model did not. The Monte-Carlo calculation used a non-divergent aperture. Only a slight difference was seen in the RBE-corrected dose in normal tissue. However, in the prostate the two fields/fraction treatment showed a 5-10% increase in the RBE corrected dose. **Conclusions:** The validation measurements indicate we were able to accurately model the MEVION s250 Proton therapy system using Monte-Carlo Calculations. This may reduce the commissioning time for other proton users. Treating a prostate patient with two fields per fraction resulted in a greater RBE advantage compared to treating with one field per fraction.

6.2. Introduction.

Monte-Carlo modeling is an important tool for understanding the behavior of therapeutic proton beams in heterogeneous media, such as a patient. A medical physicist has several options to choose from when deciding which Monte-Carlo environment to use. Examples of Monte-Carlo codes commonly used in proton therapy are MCNPX[1] and Geant4[2]. Each of these codes has the disadvantage of a steep learning curve in order

to appropriately utilize them. Additionally, the export-controlled license for MCNPX limits availability of the code.

Recognizing the need for a user-friendly general purpose Monte-Carlo code, Perl et al.[3] developed TOPAS (TOol for PArticle Simulation) under an NIH grant. The TOPAS system acts as an interface for Geant4. It was optimized for ease of use in radiation therapy applications (particularly proton therapy). Where generating Geant4 simulations requires knowledge of the C++ programming language, the input files for TOPAS are text files containing the appropriate definitions for the simulation. The TOPAS environment also limits how components are defined in order to reduce the possibility of contradictory definitions for the same component.

Because it was developed specifically for proton therapy, many of the complex parts of the proton field shaping system are provided as special component definitions in TOPAS. These parts include: the range modulator wheels/propellers, apertures, compensators, multi-leaf collimators, multi-wire ion chambers, and different types of magnets for use in spot scanning applications. Additionally, TOPAS can convert the DICOM CT image of a patient and convert the CT numbers in the image to material and density using the method described by Schneider et al.[4]

To gain confidence that our TOPAS model of the MEVION s250 proton therapy delivery system (MEVION Medical Systems Littleton, Massachusetts) is accurate in media with complex geometries (in patients), it must first be compared with measurement with simple phantom studies. This study documents the validation of our Monte-Carlo Model.

The primary motivation for developing a Monte-Carlo model of the MEVION s250 proton therapy system is the ability to extract LET information from patient treatments. It has been suggested that the increased LET near the proton's end of range should lead to an increased proton RBE.[5-9] This increased RBE at the end of range has been verified in *in vitro* studies by Belli et al.[10] and Schuff et al.[11]

Based on ICRU 78[12], the standard RBE used clinically for protons is 1.1. However, Carabe and others have suggested RBE models that are dependent on LET, dose per fraction, and tissue type.[7,13] This study concentrates on the model developed by Carabe et al.[7] to analyze the variable RBE of protons delivered to the target, and calculate the difference in the RBE-corrected dose to the patient when a subset of the planned fields are delivered for each fraction rather than all planned fields delivered in every fraction.

6.3. Methods.

A model of the MEVION s250 Proton therapy system was created in the TOPAS Monte-Carlo environment using machine geometry and field shaping system information provided by the vendor. For 17 of 24 available treatment options, validation of the TOPAS model was performed by comparing scored by TOPAS to the dose measurements obtained during commissioning of the treatment planning system. For all Monte-Carlo simulations, 10^8 particle histories were used. The measurements compared included:

- pristine peak depth-dose profiles.

- In-air profiles for a standard-sized square field (20cmx20cm or 10cmx10cm depending on the maximum field size for each option) at isocenter and at 20cm upstream and 20 cm downstream of isocenter,
- In-air profiles with a half-beam blocked aperture at isocenter and at 20cm upstream and 20 cm downstream of isocenter.
- In-water depth-dose profiles of pristine Bragg peaks.
- In-air longitudinal profiles from 20 cm upstream of isocenter to 20 cm downstream of isocenter.
- Spread-out Bragg peaks were also calculated and compared to measurement.

The CT number to material conversion for the patient plan was performed as described by Schneider et al.[4] This method is quite similar in implementation to the CT number to proton stopping power ratio conversion described by Schneider et al.[14]

The CT simulator used in this study was a Brilliance 16-slice large bore spiral CT scanner (Philips Healthcare Andover, Massachusetts). Routine quality assurance tests are regularly performed on the CT simulator to ensure their performance is consistent with the recommendations of AAPM Task Group Report 66 [15].

The CT-electron density (ED) phantom (CIRS model 062M Norfolk, VA) was scanned using a pelvis scan protocol, as shown in Figure 6.1. The scan parameters for this protocol was: 120 kVp, 300 effective mAs, collimator set to 16 x 1.5 mm, 0.5second rotation time, 0.688 pitch, standard resolution and standard filter. The phantom was scanned with a water equivalent insert at the top of the phantom (position 1) which was subsequently replaced with a titanium insert for a second set of scans. These scans were repeated with the phantom in three locations within the field of view (FOV) of the CT

scanner; in the center of the FOV, at 6 cm up and 6 cm right, and at 5 cm left and 4 cm down.

The CT scans that were acquired were then imported into our commercial treatment planning system (TPS), Eclipse v11 (Varian Oncology Systems Palo Alto, CA). CT numbers of the tissue substitute materials were measured using the area profile tool in Eclipse by recording the mean CT number within the area of interest for each material in the electron density phantom. The measured CT numbers were then sorted by the tube potential at which they were acquired and a mean CT number was calculated for each material averaged over all the phantom setups scanned.

The CT numbers and the known material properties of the tissue equivalent inserts were the imported into an in-house script. This script performed the stochiometric fitting to calculate the theoretical CT number of ICRU 44[16] human tissues which were then correlated with the physical densities of the tissues. From these values, the physical density of any given voxel in a CT image can be calculated by a linear interpolation between the two nearest ICRU 44[16] human tissues.

The chemical makeup of each voxel in the CT image is calculated via a step function. For voxels with CT numbers between -100 HU and 1149 HU, the material assignment was somewhat different. It is clear that voxels having the same CT number value as the theoretical CT number of an ICRU 44[16] human tissue should be assigned to have the chemical makeup of that ICRU 44[16] tissue. The material assignment for voxels having CT numbers not matching the theoretical CT number values of the ICRU 44[16] tissues in less clear. For these tissues the material was assigned according to ICRU 44[16] tissue with the nearest CT number value.

Special cases of the material assignment step function were required for low density and high density tissues. Voxels with a CT number less than -950 HU were assumed to be dry air. Voxels with CT number values between -950 HU and -100 HU were assigned to be lung tissue. Cortical bone tissue was assigned to voxels having CT number values between 1149 HU and 2995 HU. Any voxel with a CT number greater than 2995 HU was assigned to be titanium. Table 6.1 shows the 36 materials used in this conversion along with the range of CT numbers over which each material is assigned.

Apertures and compensators were converted from the DICOM plan into the TOPAS format via a script written in MATLAB. The apertures and compensators are defined in the DICOM RT-Plan file. The aperture definition in the RT-Plan file consists of a list of values. Each value represents alternating x- and y-coordinates of the aperture edge as it would appear if it were at isocenter. To obtain the actual aperture, these coordinates must be reduced to account for the divergence of the field.

The compensator definition is more complicated than for apertures. The compensator definition in the DICOM RT-Plan file gives the position of the first drill position, the spacing between drill positions, the number of rows and columns in the compensator, and a list of drill depths for every drill position in the compensator. The format of the list of drill depths in such that the first value in the list is the drill depth at the starting position. Each subsequent value in the drill depth list is the drill depth of the next column in the same row. When all the columns in a row are assign a drill depth, the position of the drill depth goes to the first column of the next row. This is repeated until all drill positions are assigned.

Table 6.1. The 36 materials used for the CT Number to material conversion for TOPAS with the range of CT Number values for which each material is assigned.

ICRU 44 Human Tissue	CT Number Lower Boundry	CT Number Upper Boundry
Air	-1000	-949
Lung(inflated)	-950	-99
Adipose	-100	-47
YellowMarrow	-48	-8
Breast	-9	15
RedMarrow	16	20
GITract	21	30
Lymph	31	40
Pancreas	41	44
Testis	45	47
Brain	48	50
Thyroid	51	53
Muscle	54	56
Kidney	57	57
Lung(deflated)	58	59
Ovary	60	61
EyeLens	62	65
Liver	66	67
Spleen	68	68
Blood	69	79
Heart	70	72
Skin	73	82
Cartilage	83	101
Spongiosa	102	184
Skeleton—spongiosa	185	330
Skeleton—sacrum	331	434
Skeleton—vertebral(D6-L3)	435	474
Skeleton—femur	475	531
Skeleton—ribs-2nd&6th	532	588
Skeleton—vertebral(C4)	589	628
Skeleton—humerus	629	700
Skeleton—ribs-10th	701	806
Skeleton—cranium	807	922
Skeleton—mandible	923	1148
Skeleton—cortical	1149	2994
Titanium	2995	2996

Dose and LET were scored using 10^8 histories for each field in the plan. Dose was normalized to the center of the SOBP and combined with the LET, dose per fraction, and the tissue α/β ratio to calculate the RBE corrected dose proposed by Carabe et al. (2012).

$$RBE = \frac{-(\alpha/\beta)_{photon} + \sqrt{(\alpha/\beta)^2_{photon} + 4d_{proton}\left[(\alpha/\beta)_{photon} RBE_{max} + RBE^2_{min} d_{proton}\right]}}{2d_{proton}}. \quad (1)$$

Two RBE corrected dose distributions were calculated. One assuming the dose was delivered in 30 fractions with 90 cGy delivered by each field. The other RBE-corrected dose distribution simulated 15 fractions from each field, delivering 180 cGy per fraction. The two RBE-corrected dose distributions were then compared. The two RBE corrected dose distributions were then compared in two ways. First, the RBE-corrected dose was compared over a single fraction. Then the RBE corrected dose was compared over the entire treatment.

6.4. Results.

6.4.1. Model Validation.

Figure 6.1 shows the OpenGL rendering of the TOPAS model of the field shaping system (FSS). This model includes all components of the MEVION system from the source defined at the cyclotron exit window to the compensator. The cyclotron, gantry, vault walls, and couch were not included in this model. These parts contribute only a small amount of scattered secondary radiation (gamma and neutrons) to the patient which can be neglected when measuring dose to the patient. The dimensions and location of the parts of the FSS were provided under a nondisclosure agreement with MEVION Medical Systems .

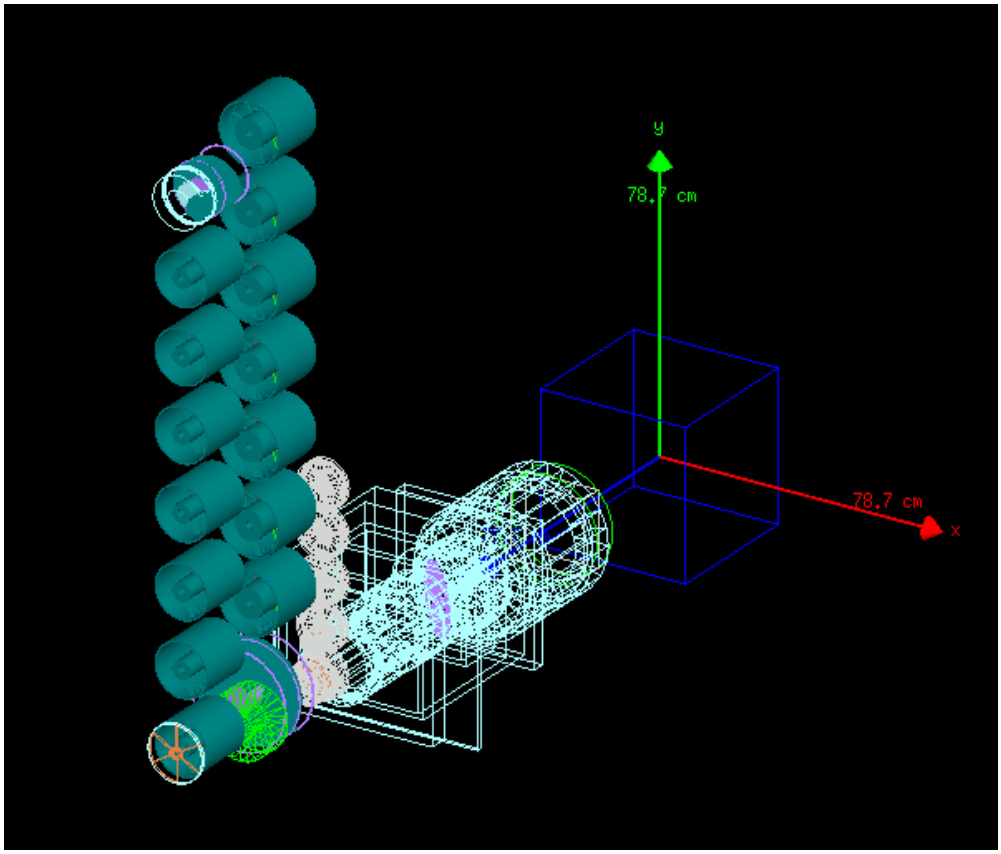

Figure 6.1. An OpenGL redering of the MEVION s250 field shaping system.

Figure 6.2 shows the depth-dose profile comparison between the TOPAS result and measurement for a single Bragg peak for 1 of the 24 (option 1) available options for the Mevion s250 system. Note the range difference between the curves is less than 1 mm. The distance between the 80% and 20% dose levels near the end of range (distal fall-off) for this curve indicates the energy spread of the proton source. In this example the TOPAS model shows a slightly larger energy spread than the measured beam. However, the resulting difference in the distal fall-off is less than 1 mm. The TOPAS calculation is significantly lower in the region proximal to the peak. This difference is

most likely due to a difference in the position of the water phantom compared to the position of the water phantom when measurements were made.

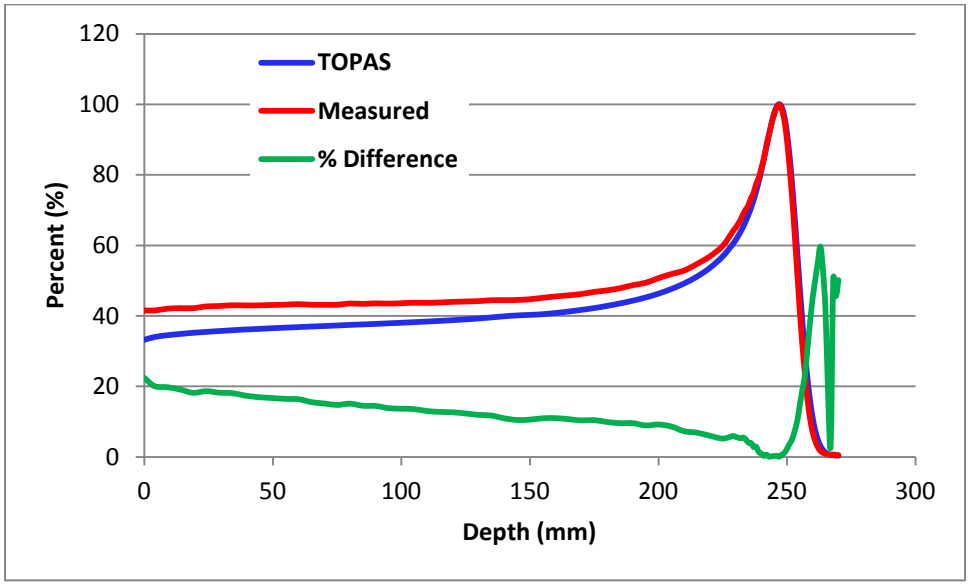

Figure 6.2. For option 1, a plot of the on depth dose profile of a 20cmx20cm field. The measured dose is in red and the TOPAS calculated dose is in blue. 10^9 histories were run for the TOPAS calculation. The percent difference between the curves is shown in green.

Figure 6.3 shows the same data as Figure 6.2 with an inverse-square correction applied to the TOPAS data. In this case, the calculated and measured depth-dose profiles are much more similar.

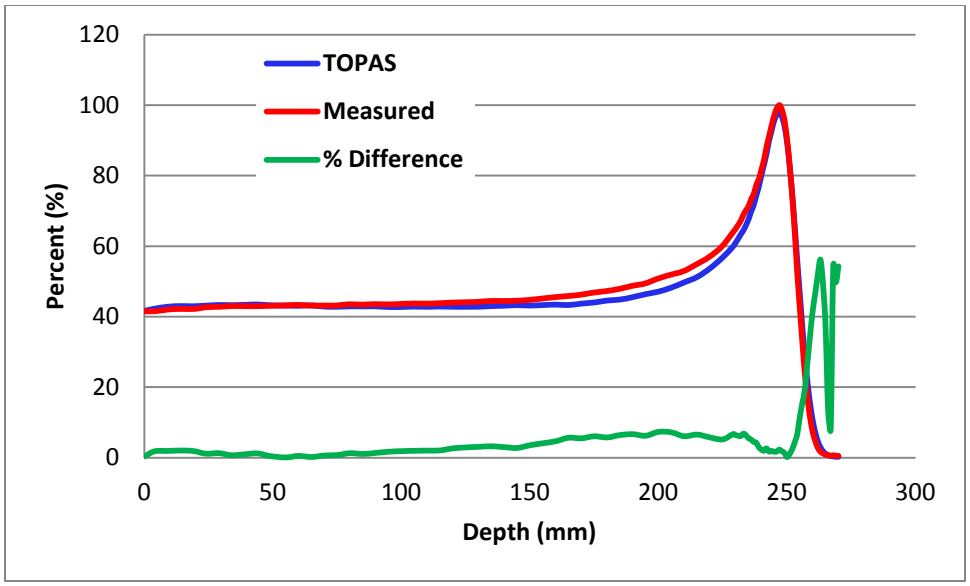

Figure 6.3. For option 1, a plot of the on depth dose profile of a 20cmx20cm field. The measured dose is in red and the TOPAS calculated dose with an inverse-square correction applied is in blue. 10^9 histories were run for the TOPAS calculation. The percent difference between the curves is shown in green.

Measurements similar to those shown in Figure 6.2 were performed for 17 of the 24 treatment configurations (options). Figure 6.4 shows a comparison of the proton range calculated by TOPAS versus the range measured during the clinical commissioning of each option. In all cases the TOPAS range matches the measured range within 1 mm. The remaining 7 options (options 18-24) were not modeled. The ranges and modulations available for options 18-24 can be modeled using options 1-12. The primary difference between the modeled and the unmodeled options is the maximum lateral field size available. Options 1-12 have a maximum field size of 25 cm. The maximum field size for options 18-24 is only 14 cm, but with a higher delivery dose rate. All treatment locations could be modeled using the first 17 options, so these options were deemed redundant, for this study.

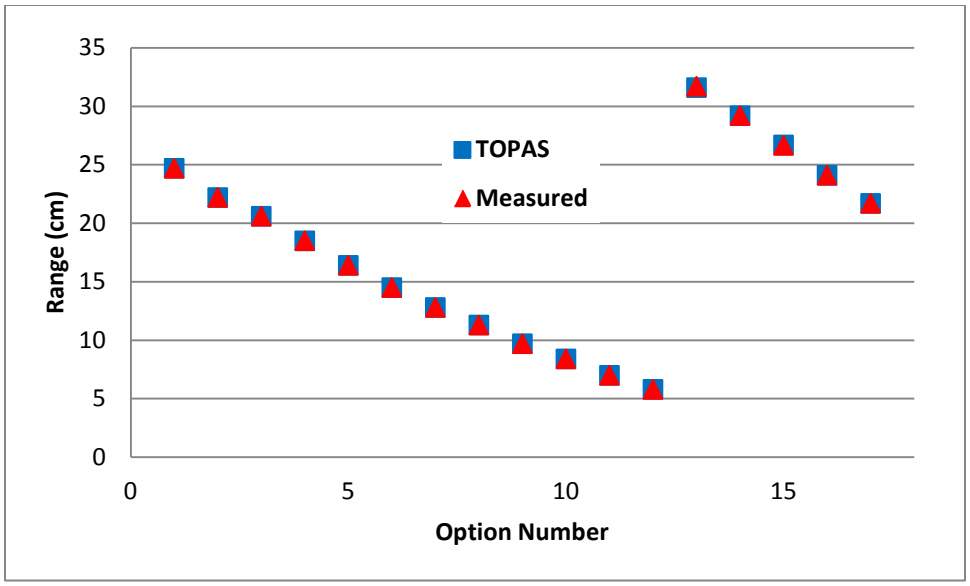

Figure 6.4. A comparison of the TOPAS calculated range vs. the measured range for 17 of 24 options for the MEVION s250 treatment system.

Figure 6.5 shows the in-air lateral profiles for option 1; the same option shown in Figure 6.2. This measurement verifies the flatness and field divergence of the field produced by the TOPAS model. A small difference was seen in the in-air profiles at doses <20%. The suspected cause of the difference was the aperture divergence. While measured data utilized a divergent aperture, the Monte-Carlo calculation used a non-divergent aperture.

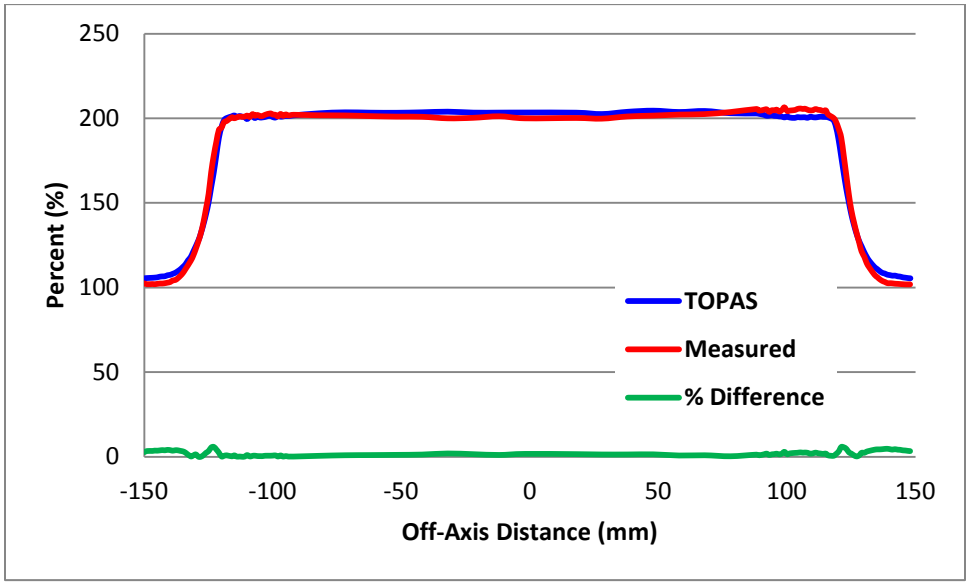

Figure 6.5. For option 1, a plot of the on in-air profile of a 20cmx20cm field at z=0cm. A 2mm shift was applied to the measured data, and the calculated data was normalized to 103%. There were 10^9 histories were run for the TOPAS calculation. The difference below 20% dose was due to the effects of divergent vs. non-divergent apertures. The measured dose is in red and the TOPAS calculated dose is in blue. The percent difference between the curves is shown in green.

Figure 6.6 show the in-air half-beam block measurements. This measurement derives the virtual source size of the TOPAS model. The virtual source size is the apparent size of the source after the beam has passed through the FSS. Lateral penumbra and field size measurements of the standard-sized square field matches the measured field within 1mm at all three planes compared. Half-beam blocked penumbra measurements matched within 1mm at the three planes compared.

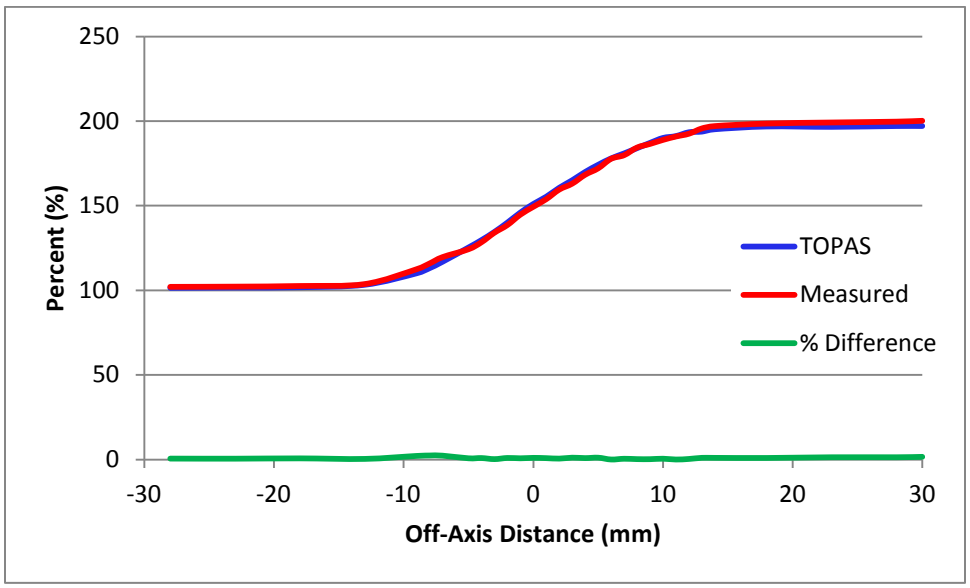

Figure 6.6. For option 1, a plot of the on axis penumbra for a half beam blocked field profile at z=20 cm. The measured dose is in red and the TOPAS calculated dose is in blue. There were 10^9 histories were run for the TOPAS calculation. A 2.5 mm shift was applied to the measured data. The measured dose is in red and the TOPAS calculated dose is in blue. The percent difference between the curves is shown in green.

Figure 6.7 shows the in-air longitudinal profiles. This measurement derives the location of the virtual source for this option. Since these curves match each other within <0.5%, it is reasonable to believe that the virtual source location according to the TOPAS model is close to matching the measured locations.

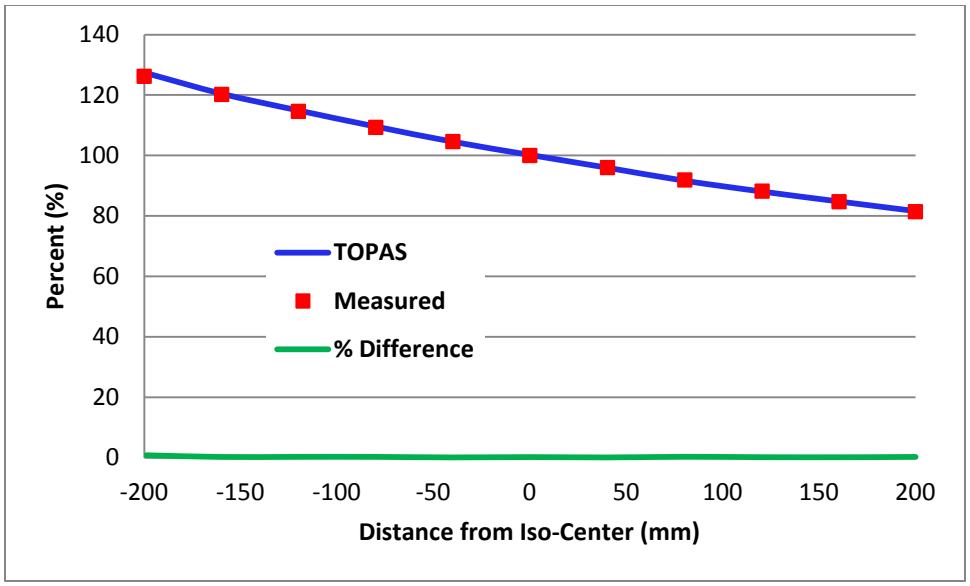

Figure 6.7. For option 1, A comparison of the in-air longitudinal profile of the TOPAS model vs the measured data. The data was normalized at isocenter and 10^9 histories were used for the TOPAS calculation. The measured dose is in red and the TOPAS calculated dose is in blue. The percent difference between the curves is shown in green.

Range measurements of the Monte-Carlo simulations matched the measured data within 1mm. The distal fall-off for the simulated fields matched within <1mm. Lateral penumbra and field size measurements of the standard-sized square and half-beam blocked fields matched within 1mm for all three planes compared.

After validating the TOPAS model versus the measured commissioning data, SOBP's were then created and compared to measure data. Figure 6.8 shows an example of such a comparison for option 15 (Range=27 cm, Modulation=10 cm). As with the other TOPAS results the distal fall-off of the calculation is slightly greater than the measured SOBP. Up to a depth of 26 cm the TOPAS calculated model matches the measured data within <2.3%. At depths between 26 and 27 cm the difference in the measured and calculated SOBP's increased to 2.5-5%. Beyond depth of 27 cm, the

difference in the measure and calculated curves increases dramatically. Two factors contributed to the increased percent difference beyond 27 cm: the larger distal falloff in the Monte-Carlo and the low dose value near the end of range of the protons.

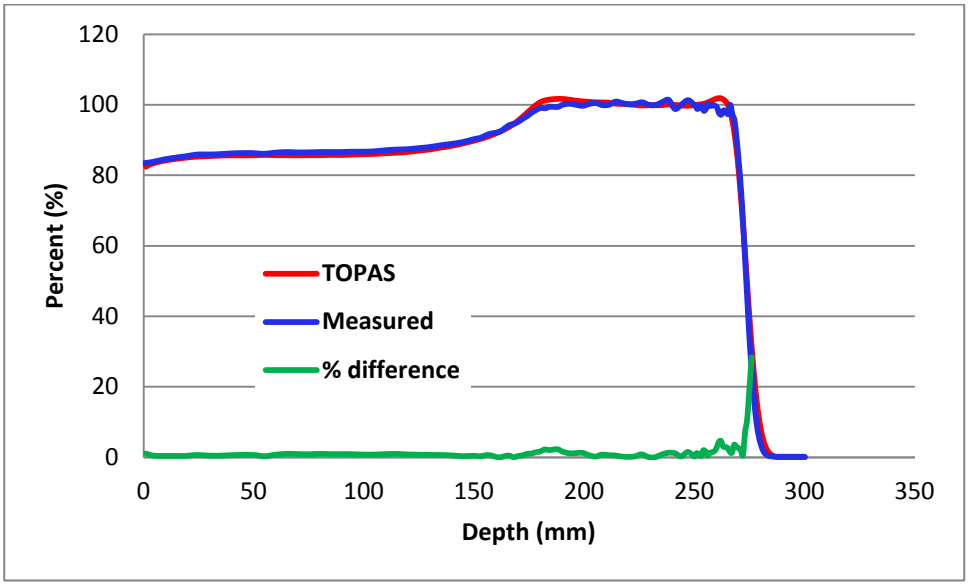

Figure 6.8. For Option 15: Range 27 cm, Mod 10 cm, A comparison of the depth-dose in water calculated by TOPAS and the dose measured in a water tank during TPS validation (10^8 histories). The measured dose is in red and the TOPAS calculated dose is in blue. The percent difference between the curves is shown in green.

6.4.2. Model Application to Treatment Delivery Regime

Figure 6.9 shows the beam arrangement of the prostate treatment plan as seen in TOPAS. The top image shows the right lateral field. The bottom image shows the left lateral field. Note the CT images are rotated by 180 degrees representing a couch rotation. The colors in the CT images represent the density and material of the tissue with red representing lower density soft tissue. White represents high density tissue and green represents intermediate density tissue.

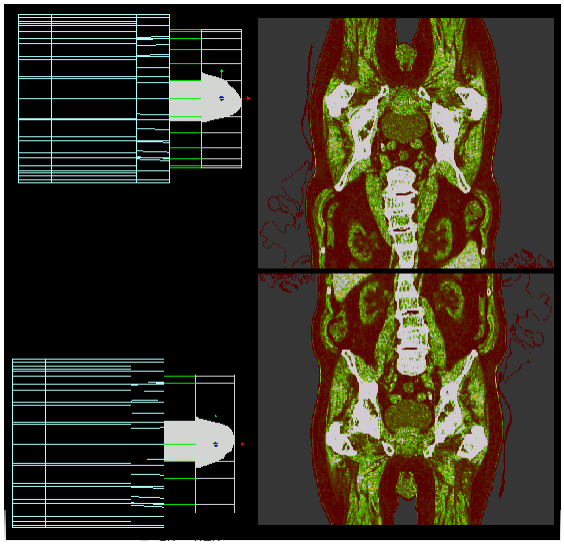

Figure 6.9. A TOPAS rendering of the setup for the two patient fields calculated in this study. Top: Left lateral field, couch rotated 180 degrees. Bottom: Right lateral field, couch at 0 degrees.

Figure 6.10 shows a comparison of the profiles of the dose and RBE-corrected dose for a single fraction of the prostate treatment. The location of this profile is through the center of the prostate across the entire patient. For the single field per fraction case in this comparison, only the right lateral field is shown. Note the entrance dose of the single field is twice the entrance dose of the two field delivery. However, the exit dose of the single field delivery is zero while in the two-field delivery the dose profile is approximately symmetric. Within the target region, the physical dose distributions are indistinguishable from each other.

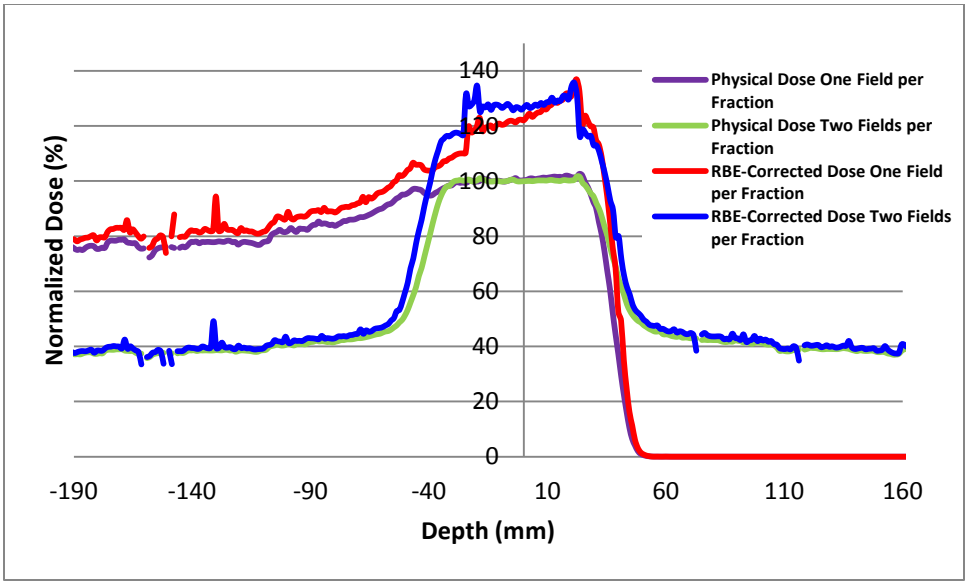

Figure 6.10. A comparison of the RBE-corrected for one field per fraction (red) and two fields per fraction (blue) for a single fraction of treatment. The profiles were calculated through the center of the target (α/β=3 in normal tissue, α/β=1.5 in the prostate). The physical dose for the one field and two fields per fraction treatment regimes are shown in purple and green, respectively.

The RBE-corrected dose distributions in a single fraction are quite different depending on the delivery mode. The RBE-corrected dose distributions show a similar relation as the physical dose in regions outside the target. However, within the target region the two-field delivery results in a much more uniform RBE-corrected dose than the single field delivery.

Over the entire treatment, the differences between the single field delivery and the two field delivery combine to result in an RBE-corrected dose that is more or less equivalent in tissues outside the target. The two field delivery shows an increased RBE-corrected dose for the prostate. A comparison of the RBE-corrected dose distributions for the same profile for the entire treatment is shown in Figure 6.11.

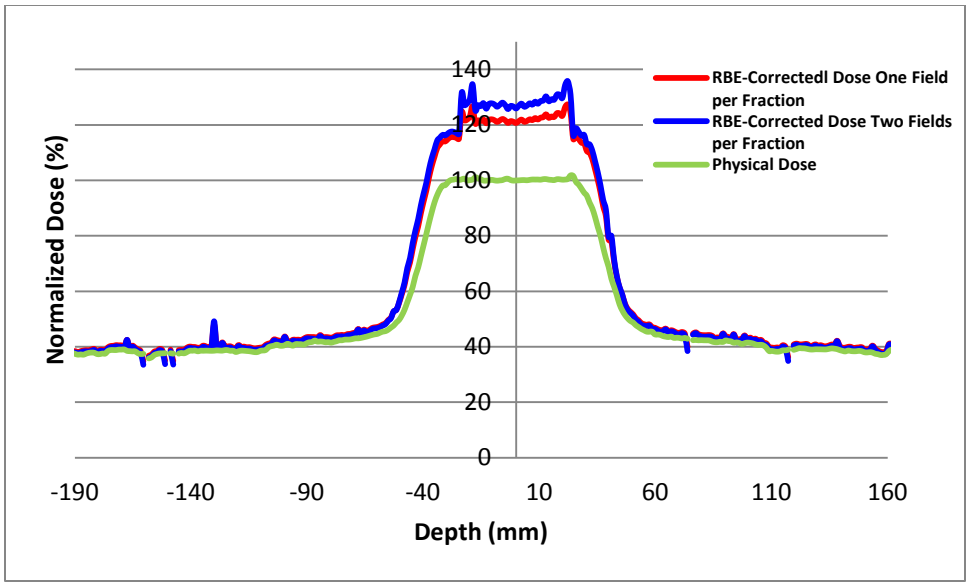

Figure 6.11. A comparison of the RBE-corrected for one field per fraction (red) and two fields per fraction (blue) for the entire treatment. The profiles were calculated through the center of the target (α/β=3 in normal tissue, α/β=1.5 in the prostate). The physical dose for the one field and two fields per fraction treatment regimes are shown in green.

6.5. Discussion.

The TOPAS validation performed in this study is sufficient for creating a Monte-Carlo model for performing general proton studies. Further validation is required in order to be able to use the TOPAS model as an accurate representation our proton delivery system. For instance, the aperture, compensator, and CT number to material conversion require further testing. In this study, the validation of these components was qualitative. Their accuracy was judged based on a visual inspection of the OpenGL rendering of the components by the TOPAS code and the resultant dose distribution produced by the TOPAS model. For possible clinical use, a quantitative validation of these components is required.

An important factor in the RBE model used in this study is the role of the α/β ratio in the calculated RBE. If the α/β ratio of the prostate were significantly different from

1.5 Gy, the difference in the RBE-corrected dose between treatment regimes could be quite different. For example, as the α/β ratio assigned to the prostate is increased up to 4 Gy, the difference in the RBE-corrected dose for the two delivery regimes decreases. At an α/β ratio value of 4 Gy there is no discernible difference in the RBE corrected dose values in the prostate. At α/β ratio values greater than 4 Gy would result in a higher RBE-corrected dose for the single field per fraction treatment.

While these α/β values are not clinically relevant for prostate, the impact of the α/β ratio on the RBE-corrected dose does provide possible implications for other tumor sites. For a brain tumor (α/β=10 Gy) treated with opposed fields, there might be an RBE advantage in treating the patient with only one field per fraction. Further investigation is merited.

6.6. Conclusion.

The depth-dose and lateral profiles measured during commissioning of the MEVION s250 proton therapy system can be adequately replicated within the TOPAS Monte-Carlo modeling environment. This modeling may reduce commissioning time for future proton users by reducing the need for beam measurements using a water tank and ionization chambers. Further, this work allows users to easily obtain proton LET information which can subsequently be used to correct for the LET dependence of the proton RBE

The RBE-corrected dose distributions for a single fraction are significantly different for the two treatment delivery strategies. Over the course of the entire treatment

the greater RBE-corrected dose uniformity of the two fields per fraction plan results in a greater RBE advantage in the prostate over the entire treatment.

Chapter 7. Conclusion

A primary reason for a clinic to only deliver a subset of the planned proton fields in a given fraction is to increase patient throughput for the clinic. The rationale for the delivery strategy is that over the course of treatment the physical dose to the target will be the same regardless of the delivery strategy. In theory, it is correct that the dose to the target will be unchanged by delivering a subset of fields. However, when uncertainties and biological influences are included the effect of delivering a subset of planned fields is called into question.

Physical uncertainties such as setup error or a heterogeneity entering/exiting the treatment field carry a higher relative weight when a subset of fields are delivered due to the lower number of distinct fields being delivered over the course of treatment. In cases where such uncertainties are large and systematic, existing in multiple fractions of the treatment, we have shown that delivering a subset of fields is more detrimental to plan quality than delivering all planned fields for every fraction.

There are two major factors contributing to the biological influences that affect the resulting treatment when different treatment delivery strategies are used. The first is purely due to the difference in the fractionation of the radiation in normal irradiated tissue. This difference was illustrated by calculating the BED of the treatment for different treatment delivery regimes. When a subset of fields was delivered for each fraction, the BED in normal tissue was significantly higher than when all planned fields

were delivered. The fewer fields that were delivered the greater the difference in the overall treatment BED.

The other biological influence affected by the treatment delivery strategy is the fact that the proton RBE may not be a constant. In fact it is dependent on LET, dose per fraction, and tissue type (represented by the α/β ratio). For a prostate ($\alpha/\beta \approx 1.5$) treatment we have shown that the variable RBE leads to a biological advantage when the prostate is treated with two fields per fraction rather than one field per fraction. However, the dependence of the proton RBE on tissue type suggests that treating a target in the brain ($\alpha/\beta \approx 10$) with opposed fields may lead to an RBE disadvantage in the target when treating two fields per fraction. The RBE disadvantage in the target in the brain treated with two fields per fraction may be offset by the decreased BED to normal brain tissue for the same treatment.

Between biological influences and physical uncertainties the greatest impact on overall treatment quality when comparing different delivery strategies comes from the biological influences. Unreasonably large physical uncertainties must be included in the treatment in order to demonstrate a small difference in treatment quality. The probability of these uncertainties occurring in an actual treatment is quite small.

However, differences due to the biological influences are due to the nature of the chosen delivery regime and are greater in magnitude than the impact of physical uncertainties. Care must be taken to avoid damage to normal tissue due to the biological effects of the treatment delivery regime. Delivering all planned fields for every fraction minimizes both the small effect caused by physical uncertainties and minimizes the BED in normal tissue.

REFERENCES

1. Y. Wang, J. A. Efstathiou, G. C. Sharp, H. M. Lu, I. F. Ciernik and A. V. Trofimov, Med Phys **38** (8), 4623-4633 (2011).

2. M. Engelsman, T. F. DeLaney and T. S. Hong, Int J Radiat Oncol Biol Phys **79** (2), 616-622 (2011).

3. A. Trofimov, P. L. Nguyen, J. A. Efstathiou, Y. Wang, H. M. Lu, M. Engelsman, S. Merrick, C. W. Cheng, J. R. Wong and A. L. Zietman, Int J Radiat Oncol Biol Phys **80** (3), 928-937 (2011).

4. E. O. Lawrence, USA Patent No. 1,948,384 (1934).

5. D. Halliday, *Introductory Nuclear Physics*, 2nd ed. (John Wiley and Sons, Inc, New York, 1955).

6. K. Gall, US Patent No. US 7,728,311 B2 (2010).

7. K. Hiramoto, H. Akiyama, K. Matsuda, T. Norimine and M. Tadakoro, USA Patent No. 6,316,776 B1 (Nov. 13, 2001).

8. U. Linz, (Springer, New York, 2012).

9. Y. Jongen, (Google Patents, 2004).

10. M. F. Moyers, D. W. Miller, D. A. Bush and J. D. Slater, Int J Radiat Oncol Biol Phys **49** (5), 1429-1438 (2001).

11. U. Schneider, E. Pedroni and A. Lomax, Physics in Medicine and Biology **41** (1), 111-124 (1996).

12. B. Schaffner and E. Pedroni, Physics in Medicine and Biology **43** (6), 1579 (1998).

13. A. Pedro, Physics in Medicine and Biology **54** (11), N205 (2009).

14. P. C. Park, X. R. Zhu, A. K. Lee, N. Sahoo, A. D. Melancon, L. Zhang and L. Dong, Int J Radiat Oncol Biol Phys **82** (2), e329-336 (2012).

15. W. Newhauser, Radiation Protection Dosimetry **133** (1), 60-62 (2009).

16. S. V. Sejpal, R. A. Amos, J. B. Bluett, L. B. Levy, R. J. Kudchadker, J. Johnson, S. Choi and A. K. Lee, Int J Radiat Oncol Biol Phys **75** (1), 40-48 (2009).

17. C. Beltran, A. Pegram and T. E. Merchant, Radiother Oncol **102** (2), 206-209 (2012).

18. C. Vargas, M. Wagner, C. Mahajan, D. Indelicato, A. Fryer, A. Falchook, D. Horne, A. Chellini, C. McKenzie, P. Lawlor, Z. Li, L. Lin and S. Keole, Int J Radiat Oncol Biol Phys **70** (5), 1492-1501 (2008).

19. M. van Herk, M. Witte, J. van der Geer, C. Schneider and J. V. Lebesque, International Journal of Radiation Oncology*Biology*Physics **57** (5), 1460-1471 (2003).

20. M. Urie, M. Goitein, W. R. Holley and G. T. Y. Chen, Physics in Medicine and Biology **31** (1), 1 (1986).

21. M. Engelsman, S. J. Rosenthal, S. L. Michaud, J. A. Adams, R. J. Schneider, S. G. Bradley, J. B. Flanz and H. M. Kooy, Medical Physics **32** (11), 3468-3474 (2005).

22. L. Hong, M. Goitein, M. Bucciolini, R. Comiskey, B. Gottschalk, S. Rosenthal, C. Serago and M. Urie, Phys Med Biol **41** (8), 1305-1330 (1996).

23. H. Paganetti, Phys Med Biol **57** (11), R99-R117 (2012).

24. H. Paganetti, A. Niemierko, M. Ancukiewicz, L. E. Gerweck, M. Goitein, J. S. Loeffler and H. D. Suit, International journal of radiation oncology, biology, physics **53** (2), 407-421 (2002).

25. C. Grassberger and H. Paganetti, Phys Med Biol **56** (20), 6677-6691 (2011).

26. H. Paganetti and T. Schmitz, Phys Med Biol **41** (9), 1649-1663 (1996).

27. A. Carabe-Fernandez, R. G. Dale and B. Jones, Int J Radiat Biol **83** (1), 27-39 (2007).

28. R. G. Dale, B. Jones and A. CÃ¡rabe-FernÃ¡ndez, Applied Radiation and Isotopes **67** (3), 387-392 (2009).

29. A. Carabe-Fernandez, R. G. Dale, J. W. Hopewell, B. Jones and H. Paganetti, Phys Med Biol **55** (19), 5685-5700 (2010).

30. B. Jones, R. G. Dale, C. Deehan, K. I. Hopkins and D. A. L. Morgan, Clinical Oncology **13**, 71-81 (2001).

31. A. Niemierko, Med Phys **24** (1), 103-110 (1997).

32. A. Niemierko, Med Phys **26**, 1101 (1999).

33. X. A. Li, M. Alber, J. O. Deasy, A. Jackson, K. W. K. Jee, L. B. Marks, M. K. Martel, C. Mayo, V. Moiseenko, A. E. Nahum, A. Niemierko, V. A. Semenenko and E. D. Yorke, Med. Phys. **39** (3), 1386-1409 (2012).

34. J. E. McGary, W. Grant and S. Y. Woo, *Applying the equivalent uniform dose formulation based on the linear-quadratic model to inhomogeneous tumor dose distributions: Caution for analyzing and reporting*. (2000).

35. F. C. Henriquez and S. V. Castrillon, J Med Phys **36** (3), 126-132 (2011).

36. R. A. Brooks, Journal of Computer Assisted Tomography **1** (4), 487-493 (1977).

37. M. Yang, G. Virshup, J. Clayton, X. R. Zhu, R. Mohan and L. Dong, Physics in Medicine and Biology **55** (5), 1343-1362 (2010).

38. R. J. Cropp, P. Seslija, D. Tso and Y. Thakur, Journal of Applied Clinical Medical Physics **14** (6), 338-349 (2013).

39. C. Bai, L. Shao, A. J. Da Silva and Z. Zhao, IEEE Transactions on Nuclear Science **50** (5 II), 1510-1515 (2003).

40. N. Hünemohr, B. Krauss, C. Tremmel, B. Ackermann, O. Jäkel and S. Greilich, Physics in Medicine and Biology **59** (1), 83-96 (2014).

41. E. C. McCullough and T. W. Holmes, Medical Physics **12**, 237-242 (1985).

42. A. A. Mustafa and D. F. Jackson, Physics in Medicine and Biology **28** (2), 169 (1983).

43. M. J. Siegel, B. Schmidt, D. Bradley, C. Suess and C. Hildebolt, Radiology **233** (2), 515-522 (2004).

44. M. F. Moyers, M. Sardesai, S. Sun and D. W. Miller, Medical Dosimetry **35** (3), 179-194 (2010).

45. S. Mutic, J. R. Palta, E. K. Butker, I. J. Das, M. S. Huq, L.-N. D. Loo, B. J. Salter, C. H. McCollough and J. V. Dyk, Medical Physics **30** (10), 2762-2792 (2003).

46. I. C. R. U. Measurements, I. C. o. R. Units and Measurements, *ICRU Report*. (International Commission on Radiation Units and Measurements., 1989).

47. M. Yang, UT 2011.

48. S. J. Thomas, Phys Med Biol **51** (6), 1491-1501 (2006).

49. J. Liebl, H. Paganetti, M. Zhu and B. A. Winey, Med Phys **41** (9), 091711 (2014).

50. B. Schaffner, Phys Med Biol **53** (6), 1545-1562 (2008).

51. A. Carabe, M. Moteabbed, N. Depauw, J. Schuemann and H. Paganetti, Phys Med Biol **57** (5), 1159-1172 (2012).

52. J. Van Dyk, K. Mah and T. J. Keane, Radiotherapy and Oncology **14** (1), 55-69 (1989).

53. J. C. Flickinger and A. Kalend, Radiotherapy and Oncology **17** (4), 339-347 (1990).

54. J. V. Lebesque and R. B. Keus, Radiotherapy and Oncology **22** (1), 45-55 (1991).

55. H. Wooten, T. Zhao, M. B. Altman, L. Santanam, S. Yaddanapudi, H. A. Gay and C. G. Robinson, International Journal of Radiation Oncology • Biology • Physics **87** (2S), S643 (2013).

56. E. D.B. Pelowitz, in *LA-CP-11-00438* (2011).

57. S. Agostinelli, J. Allison, K. Amako, J. Apostolakis, H. Araujo, P. Arce, M. Asai, D. Axen, S. Banerjee, G. Barrand, F. Behner, L. Bellagamba, J. Boudreau, L. Broglia, A. Brunengo, H. Burkhardt, S. Chauvie, J. Chuma, R. Chytracek, G. Cooperman, G. Cosmo, P. Degtyarenko, A. Dell'Acqua, G. Depaola, D. Dietrich, R. Enami, A. Feliciello, C. Ferguson, H. Fesefeldt, G. Folger, F. Foppiano, A. Forti, S. Garelli, S. Giani, R. Giannitrapani, D. Gibin, J. J. Gómez Cadenas, I. González, G. Gracia Abril, G. Greeniaus, W. Greiner, V. Grichine, A. Grossheim, S. Guatelli, P. Gumplinger, R. Hamatsu, K. Hashimoto, H. Hasui, A. Heikkinen, A. Howard, V. Ivanchenko, A. Johnson, F. W. Jones, J. Kallenbach, N. Kanaya, M. Kawabata, Y. Kawabata, M. Kawaguti, S. Kelner, P. Kent, A. Kimura, T. Kodama, R. Kokoulin, M. Kossov, H. Kurashige, E. Lamanna, T. Lampén, V. Lara, V. Lefebure, F. Lei, M. Liendl, W. Lockman, F. Longo, S. Magni, M. Maire, E. Medernach, K. Minamimoto, P. Mora de Freitas, Y. Morita, K. Murakami, M. Nagamatu, R. Nartallo, P. Nieminen, T. Nishimura, K. Ohtsubo, M. Okamura, S. O'Neale, Y. Oohata, K. Paech, J. Perl, A. Pfeiffer, M. G. Pia, F. Ranjard, A. Rybin, S. Sadilov, E. Di Salvo, G. Santin, T. Sasaki, N. Savvas, Y.

Sawada, S. Scherer, S. Sei, V. Sirotenko, D. Smith, N. Starkov, H. Stoecker, J. Sulkimo, M. Takahata, S. Tanaka, E. Tcherniaev, E. Safai Tehrani, M. Tropeano, P. Truscott, H. Uno, L. Urban, P. Urban, M. Verderi, A. Walkden, W. Wander, H. Weber, J. P. Wellisch, T. Wenaus, D. C. Williams, D. Wright, T. Yamada, H. Yoshida and D. Zschiesche, Nuclear Instruments and Methods in Physics Research Section A: Accelerators, Spectrometers, Detectors and Associated Equipment **506** (3), 250-303 (2003).

58. J. Perl, J. Shin, J. Schumann, B. Faddegon and H. Paganetti, Med Phys **39** (11), 6818-6837 (2012).

59. W. Schneider, T. Bortfeld and W. Schlegel, Physics in Medicine and Biology **45** (2), 459 (2000).

60. H. Paganetti and M. Goitein, Medical physics **27** (5), 1119-1126 (2000).

61. M. Belli, R. Cherubini, S. Finotto, G. Moschini, O. Sapora, G. Simone and M. Tabocchini, International Journal of Radiation Biology **55** (1), 93-104 (1989).

62. J. Schuff, L. Policastro, H. Duran, A. Kreiner, A. Mazal, B. Molinari, A. Burlon, M. Debray, J. Kesque and H. Somacal, Nuclear Instruments and Methods in Physics Research Section B: Beam Interactions with Materials and Atoms **187** (3), 345-353 (2002).

63. J. Wilkens and U. Oelfke, Physics in medicine and biology **49** (13), 2811 (2004).

VITA

I was first introduced to the field of medical physics in 2005 while working on my master's degree. It was through conversations with fellow students who were planning to study medical physics that my interest in the field developed. In the fall of 2009, I began studying medical physics in the accredited program at The University of Missouri.

I have been involved in two research projects. First, a master's level project involving automating mechanical quality assurance measurements using the electronic portal imager and Varian Truebeam's XML coded delivery capabilities in research mode. This project was an excellent reinforcement of testing the mechanical tolerances given in TG-142, and provided an appreciation of the time required to manually perform these tests, compared to automated methods.

In addition to this research, I spent one year performing patient specific IMRT quality assurance measurements. Performing these measurements has provided experience using measurement devices and reinforced the importance of communication between all levels of the clinical staff. The IMRT QA staff had to communicate with the physicist and physics assistants to make sure that all the QA plans for all the new patients were ready. This sometimes required waiting until late in the evening to start the QA process.

My doctoral project analyzed the effect of uncertainties on proton therapy treatment quality when the number of fields delivered daily is less than the number of fields in the

treatment plan. This project has provided insight into the importance of uncertainties in proton therapy, along with experience in treatment planning and Monte-Carlo simulation. Additionally, this project has given me an understanding of the uncertainties in the RBE of protons and the need for further research in the biological effect of protons.

While working on my doctoral research I was also able to participate in the acceptance testing and commissioning of the first single room proton therapy system. This provided extensive experience using an array of measurement tools. Being the first of its kind, it often required creative techniques in order to perform some of the required tests including: dosimetric, mechanical, safety, and neutron measurements.

My fascination with proton therapy began with the first lecture I heard on the subject during the radiation therapy physics class in my first medical physics semester. At the time, protons seemed to be the ideal treatment modality. My doctoral research, along with acceptance testing and commissioning a proton therapy system, has since removed such naivety, but my fascination with proton therapy still remains. It is my ultimate career goal to work as a board certified physicist in a radiotherapy center with cutting edge treatment options including but not limited to protons.